NON-EQUISPACED FOURIER NEURAL SOLVERS FOR PDES

Anonymous authors
Paper under double-blind review

ABSTRACT

Solving partial differential equations is difficult. Recently proposed neural resolution-invariant models, despite their effectiveness and efficiency, usually require equispaced spatial points of data. However, sampling in spatial domain is sometimes inevitably non-equispaced in real-world systems, limiting their applicability. In this paper, we propose a Non-equispaced Fourier PDE Solver (NFS) with adaptive interpolation on resampled equispaced points and a variant of Fourier Neural Operators as its components. Experimental results on complex PDEs demonstrate its advantages in accuracy and efficiency. Compared with the spatially-equispaced benchmark methods, it achieves superior performance with 42.85% improvements on MAE, and is able to handle non-equispaced data with a tiny loss of accuracy. Besides, to our best knowledge, NFS is the first ML-based method with mesh invariant inference ability to successfully model turbulent flows in non-equispaced scenarios, with a minor deviation of the error on unseen spatial points.

1 INTRODUCTION

Solving the partial differential equations (PDEs) holds the key to revealing the underlying mechanisms and forecasting the future evolution of the systems. However, classical numerical PDE solvers require fine discretization in spatial domain to capture the patterns and assure convergence. Besides, they also suffer from computational inefficiency. Recently, data-driven neural PDE solvers revolutionize this field by providing fast and accurate solutions for PDEs. Unlike approaches designed to model one specific instance of PDE (E & Yu, 2017; Bar & Sochen, 2019; Smith et al., 2020; Pan & Duraisamy, 2020; Raissi et al., 2020), neural operators (Guo et al., 2016; Sirignano & Spiliopoulos, 2018; Bhatnagar et al., 2019; KHOO et al., 2020; Li et al., 2020b;c; Bhattacharya et al., 2021; Brandstetter et al., 2022; Lin et al., 2022) directly learn the mapping between infinite-dimensional spaces of functions. They remedy the mesh-dependent nature of the finite-dimensional operators by producing a single set of network parameters that may be used with different discretizations.

However, two problems still exist – discretization-invariant modeling for *non-equispaced data* and *computational inefficiency* compared with convolutional neural networks in the finite-dimensional setting. To alleviate the first problem, MPPDE (Brandstetter et al., 2022) lends basic modules in MPNN (Gilmer et al., 2017) to model the dynamics for spatially non-equispaced data, but even intensifies the time complexity due to the pushforward trick and suffers from unsatisfactory accuracy in complex systems (See Fig. 2(a)). FNO (Li et al., 2020c) has achieved success in tackling the second problem of inefficiency and inaccuracy, while the spatial points must be equispaced due to its harnessing the fast Fourier transform (FFT).

To sum up, two properties should be available in neural PDE solvers: *(1)* discretization-invariance and *(2)* equispace-unnecessity. Property *(1)* is shared by infinite-dimensional neural operators, in which the learned pattern can be generalized to unseen meshes. By contrast, classical vision models and graph spatio-temporal models are not discretization-invariant. Property *(2)* means that the model can handle irregularly-sampled spatial points. For example, graph spatio-temporal models do not require the data to be equispaced, but vision models are equispace-necessary, and limited to handling images as 2-d regular grids. And recently proposed methods can be classified into four types according to the two properties, as shown in Fig. 1. As discussed, although the equispace-necessary methods enjoy fast parallel computation and low prediction error, they lack the ability to handle the spatially non-equispaced data. For these reasons, this paper aims to design a mesh-invariant model (defined in Fig. 1) called Non-equispaced Fourier neural Solver (NFS) with comparably low cost of computation

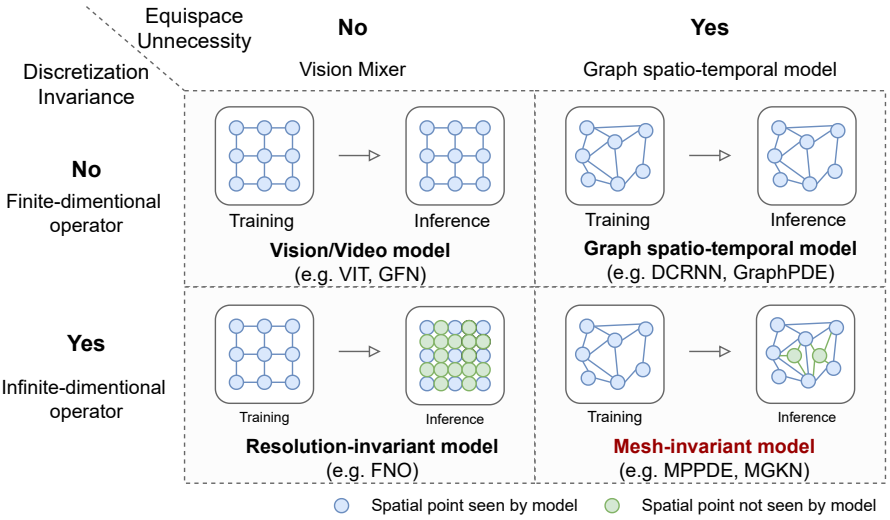

Figure 1: Four types of methods with or without the two concluded limitations.

and high accuracy, by lending the powerful expressivity of FNO and vision models to efficiently solve the complex PDE systems. Our paper including leading contributions is organized as follows:

- In Sec. 2, we first give some preliminaries on neural operators as related work, with a brief introduction to Vision Mixers, to build a bridge between Fourier Neural Operator and Vision Mixers. Thus, we illustrate our motivation for the work: To establish a mesh-invariant neural operator, by harnessing the network structure of Vision Mixers.
- In Sec. 3, we proposed a Non-equispaced Fourier Solver (NFS), with adaptive interpolation operators and a variant of Fourier Neural Operators as the components. Approximation theorems that guarantee the expressiveness of the proposed interpolation operators are developed. Further discussion gives insights into the relation between NFS, patchwise embedding and multipole graph models.
- In Sec. 4, extensive experiments on different types of PDEs are conducted to demonstrate the superiority of our methods. Detailed ablation studies show that both the proposed interpolation kernel and the architecture of Vision Mixers contribute to the improvements in performance.

2 Background and Related Work

2.1 Problem Statement

Let $D \in \mathbb{R}^d$ be the bounded and open spatial domain where n_s-point discretization of the domain D written as $\boldsymbol{X} = \{\boldsymbol{x}_i = (x_i^{(1)}, \ldots, x_i^{(d)}) : 1 \leq i \leq n_s\}$ are sampled. The observation of input function $a \in \mathcal{A}(D; \mathbb{R}^{d_a})$ and output $u \in \mathcal{U}(D; \mathbb{R}^{d_u})$ on the n_s points are denoted by $\{a(\boldsymbol{x}_i), u(\boldsymbol{x}_i)\}_{i=1}^{n_s}$, where $\mathcal{A}(D; \mathbb{R}^{d_a})$ and $\mathcal{U}(D; \mathbb{R}^{d_u})$ are separable Banach spaces of function taking values in $\mathbb{R}^{d_a}$ and $\mathbb{R}^{d_u}$ respectively. Suppose $\boldsymbol{x} \sim \mu$ is i.i.d. sampled from the probability measure μ supported on D. An infinite-dimensional neural operator $\mathcal{G}_\theta : \mathcal{A}(D; \mathbb{R}^{d_a}) \to \mathcal{U}(D; \mathbb{R}^{d_u})$ parameterized by $\theta \in \Theta$, aims to build an approximation so that $\mathcal{G}_\theta(a) \approx u$. A cost functional $\mathcal{C} : \mathcal{U}(D; \mathbb{R}^{d_u}) \times \mathcal{U}(D; \mathbb{R}^{d_u}) \to \mathbb{R}$ is defined to optimize the parameter θ of the operator by the objective

$$\min_{\theta \in \Theta} \mathbb{E}_{\boldsymbol{x} \sim \mu}[\mathcal{C}(\mathcal{G}_\theta(a), u)(\boldsymbol{x})] \approx \frac{1}{n_s} \sum_{i=1}^{n_s} \mathcal{C}(\mathcal{G}_\theta(a), u)(\boldsymbol{x}) \tag{1}$$

To establish a mesh-invariant operator, $\boldsymbol{X}$ can be non-equispaced, and the learned $\mathcal{G}_\theta$ should be transferred to an arbitary discretization $\boldsymbol{X}' \in D$, where $\boldsymbol{x} \in \boldsymbol{X}'$ can be not necessarily contained in $\boldsymbol{X}$. Because we focus on spatially non-equispaced points, when the PDE system is time-dependent, we assume that timestamps $\{t_j\}$ are uniformly sampled, which means we do not focus on temporally irregular sampling or continuous time problem (Rubanova et al., 2019; Chen et al., 2019; Çağatay Yıldız et al., 2019; Iakovlev et al., 2020).

2.2 DISCRETE FOURIER TRANSFORM

Let $\boldsymbol{k}_l = (k_l^{(1)}, \dots, k_l^{(d)})$ the l-th frequency corresponding to $\boldsymbol{X}$, with $\boldsymbol{k}_l \in \mathbb{Z}^d$. The discrete Fourier transform of $f : D \to \mathbb{R}^{d_f}$ is denoted by $\mathcal{F}(f)(\boldsymbol{k}) \in \mathbb{C}^{d_f}$, with $\mathcal{F}^{-1}$ as its inverse, then

$$\mathcal{F}(f)^{(j)}(\boldsymbol{k}_l) = \sum_{i=1}^{n_s} f^{(j)}(\boldsymbol{x}_i) e^{-2i\pi <\boldsymbol{x}_i, \boldsymbol{k}_l>}, \qquad \mathcal{F}^{-1}(f)^{(j)}(\boldsymbol{x}_i) = \sum_{l=1}^{n_s} f^{(j)}(\boldsymbol{k}_l) e^{2i\pi <\boldsymbol{x}_i, \boldsymbol{k}_l>}, \quad (2)$$

where j means the j-th dimension of f. General Fourier transforms have complexity $O(n_s^2)$. When the spatial points are distributed uniformly on equispaced grids, fast Fourier transform (FFT) and its inverse (IFFT) (Rader & Brenner, 1976) can be implemented to reduce the complexity to $O(n_s \log n_s)$.

2.3 FOURIER NEURAL OPERATOR

Neural Operators. To model one specific instance of PDEs, a line of neural solvers have been designed, with prior physical knowledge as constraints. Different from these methods, neural operators (Lu et al., 2021; Nelsen & Stuart, 2021) require no knowledge of underlying PDEs, and only data. Finite-dimensional operator methods (Guo et al., 2016; Sirignano & Spiliopoulos, 2018; Bhatnagar et al., 2019; KHOO et al., 2020) are discretization-variant, meaning that the model can only learn the patterns of the spatial points which have been fed to the model in the training process. By contrast, infinite-dimensional operator methods (Li et al., 2020b;c; Bhattacharya et al., 2021; Brandstetter et al., 2022) are proposed to be discretization-invariant, enabling the learned models to generalize well to unseen meshes with zero-shot.

Kernel integral operator method (Li et al., 2020a) is a family of infinite-dimensional operators, in which $(\mathcal{G}_\theta(a))(\boldsymbol{x}) = Q \circ v^{\mathrm{T}} \circ \cdots \circ v^1 \circ P(a)(\boldsymbol{x})$ is formulated as an iterative architecture. A higher-dimensional representation function is first obtained by $v^0 = P(a) \in \mathcal{U}(D; \mathbb{R}^{d_v})$, where P is a shallow fully-connected network. It is updated by

$$v^{\mathrm{t}+1}(\boldsymbol{x}) := \sigma(W v^{\mathrm{t}}(\boldsymbol{x}) + \mathcal{K}_\phi(a) v^{\mathrm{t}}(\boldsymbol{x})), \qquad \forall \boldsymbol{x} \in D \quad (3)$$

where $\mathcal{K}_\phi : \mathcal{A} \to \mathcal{L}(\mathcal{U})$ is a kernel integral operator mapping, mapping a to bounded linear operators, with parameters ϕ. W is a linear transform and σ is a non-linear activation function. After the final iteration, Q projects $v^{\mathrm{T}}(\boldsymbol{x})$ back to $\mathcal{U}(D; \mathbb{R}^{d_u})$.

Fourier Neural Operator (FNO) (Li et al., 2020c) as a member in kernel integral operator methods, updates the representation by applying the convolution theorem as:

$$\mathcal{K}_\phi(a) v(\boldsymbol{x}) = \mathcal{F}^{-1}(\mathcal{F}(\kappa_\phi) \cdot \mathcal{F}(v))(\boldsymbol{x}) = \mathcal{F}^{-1}(R_\phi \cdot \mathcal{F}(v))(\boldsymbol{x}), \quad (4)$$

where R_ϕ as the Fourier transform of a periodic kernel function κ_ϕ, is directly learned as the parameters in the updating process. To be resolution-invariant, FNO picks a finite-dimensional parameterization by truncating the Fourier series of both $\mathcal{F}(v)$ and R_ϕ as a maximal number of modes $k_{\max}^{(l)}$ for $1 \le l \le d$. Because the sampled spatial points are equispaced in FNO, it can conduct FFT and IFFT to get the Fourier series, which can be very efficient.

2.4 VISION MIXER AND GRAPH SPATIO-TEMPORAL MODEL

Vision Mixers (Tolstikhin et al., 2021; Rao et al., 2021; Guibas et al., 2021) are a line of models with a stack of (token mixing) - (channel mixing) - (token mixing) as their network structure for vision tasks. They are based on the assumption that the key component for the effectiveness of Vision Transformers (VIT) (Dosovitskiy et al., 2020) is attributed to the proper mixing of tokens. The defined tokens are equivalent to equispaced spatial points in the former definition, and the research on the mixing of them can be an analogy to modeling the proper interaction or message-passing patterns among spatial points. In specific, VIT uses a non-Mercer kernel function (Wright & Gonzalez, 2021) κ_ϕ to adaptively learn the pattern of message-passing through the iterative updating process

$$\begin{gathered} v^{\mathrm{t}+1}(\boldsymbol{x}) = \sigma(\mathrm{ChannelMix} \circ \mathrm{TokenMix}(v^{\mathrm{t}}(\boldsymbol{x}))); \\ \mathrm{TokenMix}(v(\boldsymbol{x})) = \sum_i \kappa_\phi(\boldsymbol{x}, \boldsymbol{x}_i, v(\boldsymbol{x}), v(\boldsymbol{x}_i)) \cdot v(\boldsymbol{x}_i); \quad \mathrm{ChannelMix}(v(\boldsymbol{x})) = W v(\boldsymbol{x}), \end{gathered} \quad (5)$$

where W is a linear transform called channel mixing layer because it transforms the input on the channel of an image whose dimension is equivalent to function dimension d_f. Note that we omit the residual connection in Eq. (3) for simplicity.

Remark. The FNO can be regarded as a member of the family of Vision Mixers. The reason is that a component in an iteration in Eq. (4) can be written as $(R_\phi \cdot \mathcal{F}(v))(\boldsymbol{x}) = R_\phi \cdot \sum_i e^{-2\pi i <\boldsymbol{x}, \boldsymbol{x}_i>} v(\boldsymbol{x}_i)$, because in the equispaced scenarios, $\boldsymbol{x}_i$ can be regarded as lying on the same grids as $\boldsymbol{k}$ after scaling. The kernel κ_ϕ is parameterized by $\kappa_\phi(\boldsymbol{x}, \boldsymbol{x}_i, v(\boldsymbol{x}), v(\boldsymbol{x}_i)) = e^{-2\pi i <\boldsymbol{x}, \boldsymbol{x}_i>}$, and the matrix multiplication of R_ϕ also performs mixing on channels. Besides, the inverse Fourier transform can also be regarded as token mixing layers, or so-called token demixing layers (Guibas et al., 2021).

However, the powerful fitting ability and efficiency of Vision Mixers are limited to being applied to non-equispaced spatial points. Another option for non-equispaced data is graph spatio-temporal models, in which interaction patterns among spatial points are modeled in a graph message-passing way (Gilmer et al., 2017; Atwood & Towsley, 2016; Defferrard et al., 2017). The mechanism is similar to the token mixing in Vision Mixers by means of the summation in Eq. (5) conducted in the predefined neighborhood of each point. Unfortunately, the graph spatio-temporal models (Seo et al., 2016; Li et al., 2018; Bai et al., 2020; Lin et al., 2021) suffer from high computational complexity and unsatisfactory accuracy in solving complex dynamical systems (such as turbulent flows).

2.5 Motivation

Since FNO belongs to Vision Mixers, this firstly raised a question to us: *Do models employing Vision Mixers's architecture have the potential to model complex PDE systems?* Thus, experiments are conducted to give an intuitive explanation of our motivation as shown in Fig. 2. The data are generated by Navier-Stokes equations. It is noted that graph spatio-temporal methods can also handle the equispaced data. Detailed setup is given in Sec. 4.

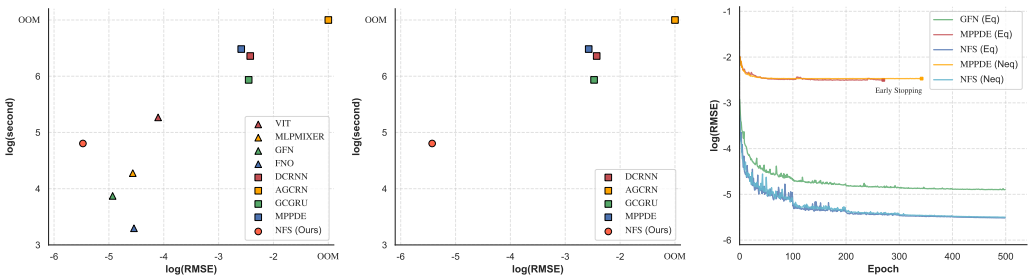

(a) Equispaced comparison (b) Non-equispaced comparison (c) Loss on Validation Set

Figure 2: Intuitive explanation of our motivation: In (a) and (b), '△' represents Vision Mixers, '□' represents graph spatio-temporal models and '◯' is the proposed NFS. In (c), 'Eq' and 'Neq' mean the methods are trained in equispaced and non-equispaced scenarios respectively.

We find that *(1)* All of the evaluated Vision Mixers are able to model the dynamical systems effectively, in spite of FNO as the only discretization-invariant model; *(2)* The complex dynamics of the systems are hardly captured by graph spatio-temporal models, whose performance on both accuracy and computational efficiency is very unsatisfactory in either equispaced or non-equispaced scenarios. Fig. 2(c) shows the problem of infeasibility of graph spatio-temporal models through the loss curves on the validation set, compared with Vision Mixers. However, Vision Mixers fail to handle the non-equispaced data. Therefore, we aim to *(1)* establish a **mesh-invariant** model, by harnessing the network structure of Vision Mixers to achieve competitive **efficiency** and **effectiveness** in equispaced scenarios, as shown in Fig. 2(a); *(2)* Besides, it should allow applicability and comparable accuracy in **non-equispaced** scenarios for solving PDEs, as shown in Fig. 2(b).

3 Proposed Method

3.1 Non-equispaced Fourier Transform

Nonuniformly signals are unavoidable in certain real-world physics scenarios, such as signals obtained by meteorological stations on the earth surface, which urge the fast Fourier transform (FFT) to be extended to non-equispaced data with efficient implementation of FFT. Non-equispaced FFTs usually rely on a mixture of interpolation and the judicious use of FFT, where the calculations of interpolation are no more than $O(n_s \log n_s)$ operations (Kalamkar et al., 2012; Cheema et al., 2017). For example, Lagrange interpolation is used to approximate the signal values on m_s resampled equispaced points

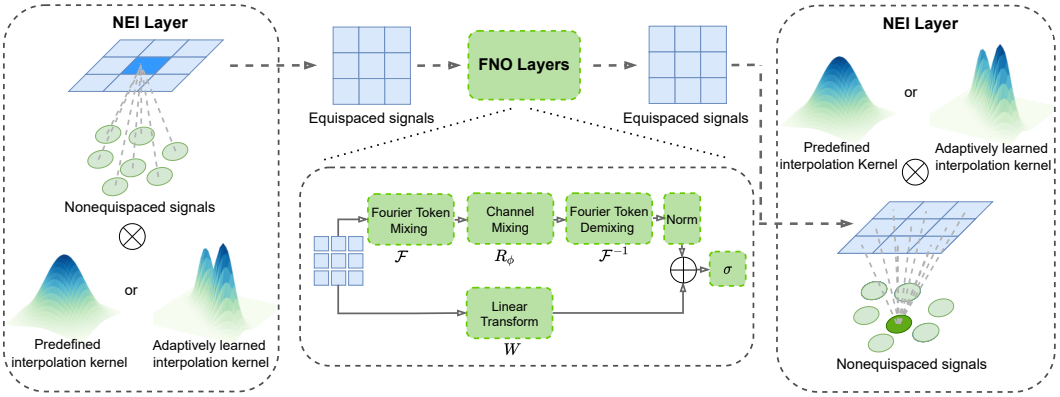

Figure 3: The architecture of NFS: In non-equispaced inperpolation (NEI) layers, the interpolation kernels are adaptively learned rather than predefined, and the interpolated equispaced signals are processed through a stack of FNO layers with the same structure of Vision Mixers.

$\{\boldsymbol{x}_j\}_{1\leq j\leq m_s}$, and then implement FFT on the interpolated points. A low rank approximation with complexity of $O(n_s \log(1/\epsilon))$ is used to replace the interpolation with complexity of $O(n_s^2)$ with ϵ as the precision of computations (Dutt & Rokhlin, 1995). Another example is commonly used Gaussian-based interpolation (Kestur et al., 2010). Denote $\mathcal{F}$ as equispaced FFT in particular, and $\mathcal{H}$ as the interpolation operator, and the proposed non-equispaced FFT can be written as

$$(\mathcal{F}\circ\mathcal{H}(f))(\boldsymbol{k}) \approx \sqrt{\frac{\pi}{\tau}} e^{\tau<\boldsymbol{k},\boldsymbol{k}>} \sum_{j=1}^{m_s} e^{-2i\pi<\boldsymbol{k},\boldsymbol{x}_j>} \sum_{i=1}^{n_s} f(\boldsymbol{x}_i) h_\tau(\boldsymbol{x}_i - \boldsymbol{x}_j). \tag{6}$$

$\mathcal{H}(f)(\boldsymbol{x}_j) = \sum_{i=1}^{n_s} f(\boldsymbol{x}_i) h_\tau(\boldsymbol{x}_i - \boldsymbol{x}_j)$ interpolates values on resampled points via convolution with the periodic heat kernel $h_\tau(\boldsymbol{x}-\boldsymbol{y}) = \sum_{\boldsymbol{l}\in\mathbb{Z}^d} e^{-(\boldsymbol{x}-\boldsymbol{l})^2/4\tau}$, with τ as a constant. Multiplication of the inperploation matrix $(H_\tau)_{i,j} = h_\tau(\boldsymbol{x}_i - \boldsymbol{x}_j)$ and the signal vector $(\boldsymbol{f})_i = f(\boldsymbol{x}_i)$ includes $O(n_s m_s) \approx O(n_s^2)$ operations. For the kernel h_τ, it is a summation of Gaussian kernel, and convolution with a single Gaussian in each points $\boldsymbol{x}_i$'s neighborhood $\mathcal{N}(\boldsymbol{x}_i)$ can yeid a tiny error depending on τ, so the interpolation operator can be approximate via $\mathcal{H}(f)(\boldsymbol{x}_j) = \sum_{\boldsymbol{x}_j\in\mathcal{N}(\boldsymbol{x}_i)} f(\boldsymbol{x}_i) h_\tau(\boldsymbol{x}_i - \boldsymbol{x}_j)$. Restricting the neighbor number to $|\mathcal{N}(\boldsymbol{x}_i)| \leq \log n_s$ leads the complexity to reduce to $O(n_s \log n_s)$.

3.2 Non-equispaced Fourier Neural PDE Solver

Non-equispaced interpolation. To harness the effectiveness of FNO, we use non-equispaced Fourier token mixing instead of the equispaced one. It generalizes the equispaced FFT in Eq. (4) as

$$\tilde{\mathcal{F}}(v) = (\mathcal{F}\circ\mathcal{H}_\eta(a))(v). \tag{7}$$

We denote $\mathcal{H}_\eta : \mathcal{A} \to \mathcal{L}(\mathcal{U})$ as the interpolation operator mapping, which maps parametric function to a bounded interpolation operator. $\mathcal{H}_\eta(a)$ gets the inerploated values on m_s resampled equispaced points via the convolution with kernel h_η as

$$(\mathcal{H}_\eta(a)v)(\boldsymbol{x}_j) = \frac{1}{n_s}\sum_{i=1}^{n_s} v(\boldsymbol{x}_i) h_\eta(\boldsymbol{x}_j - \boldsymbol{x}_i, \boldsymbol{x}_i, a(\boldsymbol{x}_i)), \tag{8}$$

where $\boldsymbol{x}_j$ lies on resampled equispaced grids. Another $\mathcal{H}'_\zeta$ interpolates back on the n_s non-equispaced ones in the same way via the convolution with kernel h_ζ. To reduce the operations to no more than $O(n_s \log n_s)$, the summation is restricted in the neighborhood of $\boldsymbol{x}_i$ and $\boldsymbol{x}_j$, such that $|\mathcal{N}(\boldsymbol{x}_i)| \approx |\mathcal{N}(\boldsymbol{x}_j)| \leq c \log n_s$ with c as a predefined constant determining the neighborhood size of spatial points. We formulate the kernel with a shallow feed-forward neural networks. Thanks to the universal approximation of neural networks, the following theorem assures that the interpolation operator can approximate the representation function v arbitrarily well. (For detailed proof, see Appendix. A.3.)

Theorem 3.1 (Approximation Theorem of the Adaptive Interpolation)**.** *Assume the setting of* ***Theorem A2*** *in Appendix. A.3 is satisfied. μ is the probability measure supported on D. For $v \in \mathcal{U}$, suppose $\mathcal{U} = L^p(D;\mathbb{R}^{d_v})$, for any $1 < p < \infty$. Then, given $\epsilon > 0$, there exist a neural network $h_\eta : \mathbb{R}^d \times \mathbb{R}^d \times \mathbb{R}^{d_a} \to \mathbb{R}^{d_v}$, such that $||\hat{v} - v||_{\mathcal{U}} \leq \epsilon$, where $\hat{v}(\boldsymbol{x}) = \int_D h_\eta(\boldsymbol{x}-\boldsymbol{y}, \boldsymbol{x}, a(\boldsymbol{y}))v(\boldsymbol{y})d\mu(\boldsymbol{y})$.*

Applicability of Layer-Norm. As shown in Fig. 3, besides the comparison of the proposed interpolation operator with the traditional ones, a notable difference between the original FNO and FNO layers in our Vision Mixer architecture is the applicability of normalization layers (Layer-Norm) which is usually used in Vision Mixers' architecture. FNO cannot adapt Layer-Norm layers, because the change of resolution will make the trained normalization parameters and spatial points disagree with each other. In comparison, the resampled equispaced points are fixed in our architecture, no matter how the discretization of the input changes. Therefore, the normalization layers can be added, in a similar way to Vision Mixers, bringing considerable improvements (See Sec. 4.3).

Mesh invariance. In the intermediate layers, which adopt equispaced FNO, the resampled points are fixed in both training and inference process, invariant to the input meshes. In the interpolation layers, the operator $\mathcal{H}_\eta(a)$ is discretization-invariant because the kernel can be inductively obtained by the newly observed signals $a(\boldsymbol{x})$, its coordinate $\boldsymbol{x}$ and resampled spatial points' relative coordinates $\boldsymbol{x}_j - \boldsymbol{x}$. In the same way, $\mathcal{H}'_\zeta(a)$ is also mesh-invariant. This allows the NFS to achieve zero-shot mesh-invariant inference ability, which is demonstrated in Sec. 4.2.

Complexity analysis. The complexity of FNO is $O(n_s \log n_s + n_s k_{\max})$. In the interpolation layers, because the interpolated values of resampled points are determined by their neighbors, we set the size of each resampled point's neighborhood in $\mathcal{G}$ and observed non-equispaced points's neighborhood in $\mathcal{G}'$ as $|\mathcal{N}(\boldsymbol{x}_i)| \approx |\mathcal{N}(\boldsymbol{x}_j)| \leq c \log(n_s)$, for $1 \leq i \leq n_s, 1 \leq j \leq m_s$. And in this way, the sparsity of the interpolation matrix reduces the complexity of the two interpolation layers to $O(c \cdot n_s \log n_s + c \cdot m_s \log n_s)$. If we set the resampled points number as n_s, the overall complexity is $O(2c \cdot n_s \log n_s + n_s \log n_s + n_s k_{\max}) \sim O(n_s \log n_s + n_s k_{\max})$.

3.3 Further Discussion

Relation to Vision Mixer. The interpolation can be compared to patchwise embedding in Vision Mixers. For example, MLPMixer learns the token mixing patterns adaptively with a feed-forward network, but the high resolution of input images does not permit the global mixing of tokens due to the complexity of $O(n_s^2)$. Therefore, the input images are firstly rearranged into patches, with each patch containing n_p pixels. In this way, the complexity is reduced to $O(n_s^2/n_p^2)$, enabling feasible token mixing. The patchwise embedding is very similar to interpolating the values on resampled points, as the former one first chooses patches' centers as n_s^2/n_p^2 resampled points, and 'interpolates' the resampled points by lifting the embedding dimension and the rearranging of their neighbors' values as the interpolated values, rather than using a kernel.

Relation to multipole graph model. The adaptively learned interpolation layer in NFS has a similar formulation of multipole graph models (Li et al., 2020b). In multipole graph models, the high-level nodes aggregate messages from their low-level neighbors as $v^{\text{High}}(\boldsymbol{x}_j) = \frac{1}{|\mathcal{N}(\boldsymbol{x}_j)|} \sum_{\boldsymbol{x}_i \in \mathcal{N}(\boldsymbol{x}_j)} v^{\text{Low}}(\boldsymbol{x}_i) h_\eta(\boldsymbol{x}_j, \boldsymbol{x}_i, a(\boldsymbol{x}_j), a(\boldsymbol{x}_i))$. Compared to multipole graph models, the values of high-level resampled equispaced nodes are approximated with low-level non-equispaced nodes' values in NFS, but nodes' values of low levels are given in multipole graphs. This causes differences in multipole graph models' message-passing and NFS's interpolation: In the former one, messages flow circularly among different levels of nodes, while in NFS, messages only exchange twice between the nodes of two levels – one is from low-level non-equispaced nodes to high-level resampled equispaced nodes, and the other is the opposite.

4 Experiments

4.1 Experiemntal Setup

Benchmarks for comparison. For finite-dimensional operators, we choose Vision Mixers including ViT (Dosovitskiy et al., 2020), GFN (Rao et al., 2021) and MLPMixer (Tolstikhin et al., 2021) as equispaced problem solvers, and graph spatio-temporal models including DCRNN (Li et al., 2018), AGCRN (Bai et al., 2020) and GCGRU (Seo et al., 2016) as non-equispaced problem solvers. For infinite-dimensional operators, the state-of-the-art FNO (Li et al., 2020c) for equispaced problems and MPPDE (Brandstetter et al., 2022) for non-equispaced problems are chosen. A brief introduction for these models is shown in Appendix. B.1. In Vision Mixers, the different timestamps in temporal axis are also regarded as 'tokens' in that timestamps are uniformly sampled.

Protocol. The widely-used metrics - Mean Absolute Error (MAE) and Root Mean Square Error (RMSE) are deployed to measure the performance. The reported mean and standard deviation of metrics are obtained through 5 independent experiments. All the models for comparison are trained with target function of MSE, i.e. $\mathcal{C}(u, v)(\boldsymbol{x}) = ||u(\boldsymbol{x}) - v(\boldsymbol{x})||^2$ corresponding to Eq. (1), and optimized by Adam optimizer in 500 epochs. The hyper-parameters are chosen through a carefully tuning on the validation set. Every trial is implemented on a single Nvidia-V100 (32510MB).

4.2 Numerical Experiments

Data. We choose four equations for numerical experiments, three of which are time-dependent (KdV, Burgers' and NS), while the other one is not (Darcy Flows). For 1-d problem, we consider Korteweg de Vries (KdV) (given in Appendix. B.2.) and Burgers' equation:

$$\partial_t u(x,t) + \partial_x u^2(x,t)/2 - \nu \partial_x^2 u^2(x,t) = 0, \tag{9}$$

where $x \in [0,1], t \in [0,1]$. $u(x,0) = u_0(x)$ is the initial condition and $\nu \in \mathbb{R}^+$ is the viscosity coefficient. For 2-d PDEs, we consider Darcy Flow (given in Appendix. B.2.) and Navier-Stokes (NS) equation for a viscous, incompressible fluid in vorticity form on the unit torus:

$$\begin{aligned} \partial_t w(\boldsymbol{x},t) + u(\boldsymbol{x},t) \cdot \nabla w(\boldsymbol{x},t) &= \nu \Delta w(\boldsymbol{x},t) + f(\boldsymbol{x}), \\ \nabla \cdot u(\boldsymbol{x},t) = 0, \qquad w(\boldsymbol{x},0) &= w_0(\boldsymbol{x}), \end{aligned} \tag{10}$$

where $\boldsymbol{x} \in [0,1]^2, t \in [0,1]$. u is the velocity field, $w = \nabla \times u$ is the vorticity, w_0 is the initial vorticity, $\nu \in \mathbb{R}^+$ is the viscosity coefficient, and f is the forcing function.

The total number of instances is 1200, with percentages of 0.7, 0.1 and 0.2 for training, validating and testing, respectively. The original simulated resolutions of PDE signals are 128×128 in NS equation. For others, see Appendix. B.2. When evaluating their performance in equispaced scenarios of different resolutions, we can downsample the resolution for training to low-resolution data, e.g. 64×64 in NS equation. To evaluate their performance in non-equispaced scenarios of different meshes, we randomly choose n_s spatial points for training.

Table 1: MAE($\times 10^{-3}$) comparison with vision mixer benchmarks.

	Burgers' ($n_t = 10$)			Darcy Flow			NS ($n_t = 1$)			NS ($n_t = 10$)		
r	512	512	1024	64	128	256	64	64	128	64	64	128
n_t'	10	40	20	1	1	1	10	40	20	10	40	20
VIT	0.5042	2.4269	1.5327	0.5073	0.9865	1.1078	9.3797	22.8565	15.7398	3.9609	12.3433	9.3010
MLPMixer	0.1973	0.4210	0.3303	0.4970	0.8909	0.9125	7.5246	15.8632	14.9360	3.1530	7.9291	7.7410
GFN	0.2383	0.4187	0.3500	0.4739	0.8659	0.9618	3.5524	10.2250	6.3976	1.7396	5.4464	3.1261
FNO	0.0978	0.1815	**0.1430**	0.4289	0.7086	0.9075	3.3425	8.9857	4.4627	2.4076	7.6979	3.7001
NFS	**0.0958**	**0.1708**	0.1474	**0.1497**	**0.2254**	**0.4216**	**1.7425**	**4.7882**	**2.6988**	**0.8636**	**3.1122**	**1.8406**

Table 2: MAE($\times 10^{-3}$) comparison with graph spatio-temporal benchmarks.

	Burgers' ($n_t = 10$)			Darcy Flow			NS ($n_t = 1$)			NS ($n_t = 10$)		
n_s	512	512	256	4096	16384	1024	4096	4096	1024	4096	4096	1024
n_t'	10	40	20	1	1	1	10	40	20	10	40	20
DCRNN	2.6122	8.5880	4.6126	1.7629	OOM	1.8146	30.6756	88.3382	52.1290	8.7025	59.6602	27.1069
AGCRN	4.6667	15.6143	10.4900	1.7336	OOM	1.6938	OOM	OOM	59.9393	OOM	OOM	42.4197
GCGRU	1.6643	5.7653	3.1400	1.7403	OOM	1.7633	28.8537	85.9303	49.9352	6.3570	57.2493	21.3537
MPPDE	1.1271	4.1213	2.4554	0.5608	0.6384	0.6673	8.9810	54.2387	20.7453	5.4353	42.3057	17.5902
NFS	**0.1085**	**0.1983**	**0.1634**	**0.1430**	**0.2379**	**0.1727**	**2.1992**	**4.7865**	**3.9178**	**0.9335**	**3.2768**	**1.8239**

Performance comparison. In this part, for time-dependent PDEs, our target is to map the observed physical quantities from initial condition $u(\boldsymbol{X}, \boldsymbol{T}) \in \mathbb{R}^{n_s \times n_t}$, where $\boldsymbol{T} = \{t_i : t_i < T\}_{1 \le i \le n_t}$, to quantities at some later time $u(\boldsymbol{X}, \boldsymbol{T'}) \in \mathbb{R}^{n_s \times n_t'}$, where $\boldsymbol{T'} = \{t_i : T < t_i < T'\}_{1 \le i \le n_t'}$. We set the input timestamp number n_t as 1 (initial state to future dynamics) and 10 (sequence to sequence), and prediction horizon n_t' as 10, 20 and 40 as short-, mid- and long-term settings. For Darcy Flows, which are independent of time, we directly build an operator to map a to u. In equispaced scenarios, the resolution is denoted by $r^d = n_s$, where d is the spatial dimension. In non-equispaced scenarios, the spatial points number is denoted by n_s. The comparison of benchmarks with or without equispace-unnecessity are shown in Table. 1 and 2 respectively, and detailed results including KdV equations with RMSE and standard deviations are given in Appendix. B.3. It can be concluded that *(1)* In equispaced scenarios, the proposed NFS obtains the lowest error in most 1-d PDE settings, and in solving 2-d PDEs, its superiority over other Vision Mixers are significant, with 42.85% improvements

on MAE according to the trials of NS ($r = 64, n_t = 10, n'_t = 40$). *(2)* In non-equispaced scenarios, the evaluated graph spatio-temporal models' performance is unsatisfactory, especially in NS equations. In comparison, NFS achieves comparable high accuracy to the equispaced scenarios, for instance, according to columns of NS ($r = 64, n_t = 10, n'_t = 40$) with ($n_s = 4096, n_t = 10, n'_t = 40$). *(3)* In some trials such as Burgers' ($n_t = 1$) in Table. B4 in Appendix. B.3, Vison Mixers including FNO also suffer from non-convergence of loss; while NFS can still generate accurate predictions. The explanation of the phenomenon will be our future work.

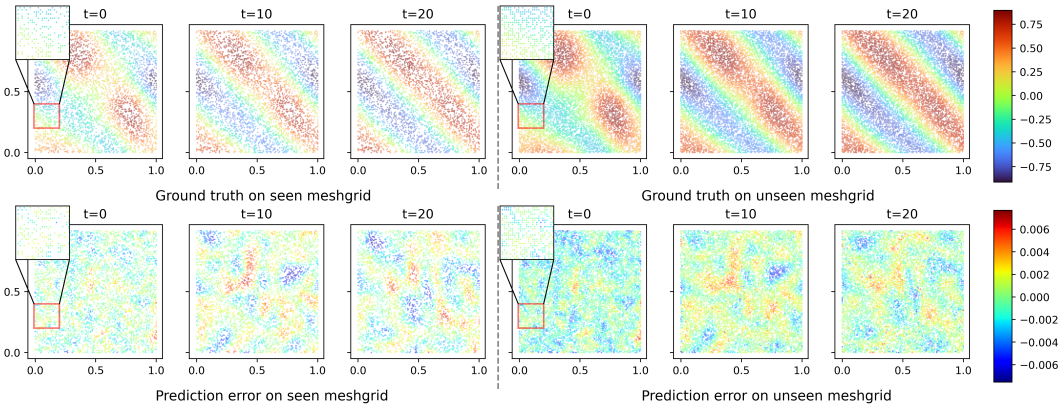

Figure 4: Visualization on non-equispaced NS equation: The training mesh ($n_s = 4096$) differs from the mesh in inference process ($n'_s = 8192$). Appendix. B.4 gives more visualization.

Table 3: Results on NS equation: MAE($\times 10^{-3}$) of NFS and different variants of NFS on seen and unseen meshes. 'Flex + LN' is the proposed NFS. 'Flex' represents the flexible interpolation layer defined in Eq. (8), 'LN' is the Layer-Norm and 'Gaus' is the predefined Gaussian interpolation. Appendix. B.5 gives details and results on other equations.

	$(n_s = 4096, n_t = 10, n'_t = 10)$			$(n_s = 1024, n_t = 10, n'_t = 20)$			$(n_s = 4096, n_t = 10, n'_t = 40)$		
n'_s	Flex + LN	Gaus + LN	Flex + ~~LN~~	Flex + LN	Gaus + LN	Flex + ~~LN~~	Flex + LN	Gaus + LN	Flex + ~~LN~~
n_s	0.9335	1.6341	1.2138	1.8239	2.1976	2.5119	3.2768	3.6422	5.6761
$2n_s$	0.9731	2.8589	1.4882	2.3530	3.7465	7.0203	3.5439	3.9092	5.8975
$3n_s$	1.1071	3.4513	1.6384	2.5179	5.7712	7.9177	3.6584	4.2102	6.6622
$4n_s$	1.1015	3.4357	1.6975	2.5919	5.5990	7.1962	3.6608	4.2628	6.6951

Mesh-invariance evaluation. We use $(u(\boldsymbol{X}, \boldsymbol{T}), u(\boldsymbol{X}, \boldsymbol{T'}))$ as the training set, and evaluate the model's performance of mesh-invariant inference ability on $\boldsymbol{X'}$, where $|\boldsymbol{X'}| = n'_s$. $\boldsymbol{X'}$ is a different mesh with $\boldsymbol{X} \subseteq \boldsymbol{X'}$. The visualization results of NS ($n_s = 4096, n'_t = 40$) are shown in Fig. 4. For a fixed n'_s, we randomly sampled different $\boldsymbol{X'}$ for 100 times, to get the mean errors and standard deviations (given in Appendix. B.5) of different spatial meshes. We can conclude from Table. 3 that *(1)* The errors on unseen meshes are larger than the errors on seen meshes, showing the overfitting effects. However, the errors on unseen meshes are acceptable, since they are even lower than other models' prediction error on seen meshes. *(2)* Larger n'_s leads to higher prediction error because a large number of unseen points are likely to disturb the learned token mixing patterns. On the other hand, NS ($n_s = 1024, n'_t = 10$) implies that small spatial point numbers of training meshes (n_s) hinder model's generalizing ability on unseen meshes, due to excessive loss of spatial information.

4.3 Architecture Analysis

Two modules in NFS differ from FNO. The first is the interpolation layers at the beginning and the end of the architecture. The second is the extra Layer-Norm in the FNO layers, which can be applicable in NFS thanks to its fixed resampled equispaced points, but inapplicable to FNO for preserving its resolution-invariance. We aim to figure out what makes NFS outperform FNO.

Effects of neighborhood sizes. It is widely believed that modeling the long-range dependency among tokens brings improvements (Naseer et al., 2021; Tuli et al., 2021; Mao et al., 2021). By contrast, some local kernel methods demonstrate their superiority (Yang et al., 2019; Liu et al., 2021; Chu et al., 2021; Park & Kim, 2022). For this reason, we first conjecture that the large neighborhood sizes in the interpolation layer are conducive to predictive performance.

Besides, as demonstrated in Sec. 3.3, the patchwise embedding in Vision Mixers can be an analogy to the resampling and interpolating, so we further establish a patchwise FNO (PFNO), with patch size equaling to 4 and $[4, 4]$ in 1-d and 2-d PDE problems, equivalent to each resampled points aggregating 4 and 16 points in spatial domains in 1-d and 2-d situations respectively. Layer-Norm is stacked in the FNO layers in PFNO, for a fair comparison. Results of Fig. 5 show that the long-range dependency may even compromise the performance, as larger mean neighborhood sizes often cause higher errors. However, no matter how large is the neighbor size, the NFS outperforms PFNO. More details are given in Appendix. B.6. Therefore, we rule out the possibility of performance gains brought form large neighborhood sizes and suppose that proposed kernel interpolation layers are the key, and is superior to the simple patchwise embedding methods.

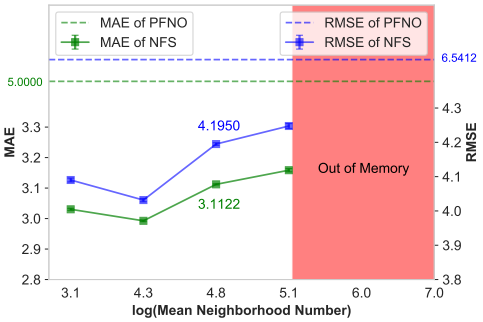

Figure 5: Effects of neighborhood sizes on NS ($r = 64, n'_t = 10, n'_t = 40$).

Benefits from learned interpolation kernel. Since the kernel interpolation is likely to hold the key to improvements, we investigate the performance gains brought from adaptively learned interpolation kernels over the predefined one (See Fig. 3). We use an inflexible Gaussian kernel $h(\boldsymbol{x}_j - \boldsymbol{x}_i) = \beta \exp(-(\boldsymbol{x}_j - \boldsymbol{x}_i - \boldsymbol{\mu})^T (\Gamma)^{-1} (\boldsymbol{x}_j - \boldsymbol{x}_i - \boldsymbol{\mu}))$ as a predefined one as discussed in Sec. 3.1, where $\Gamma = \mathrm{diag}(\gamma^{(1)}, \dots, \gamma^{(d)})$, and $\boldsymbol{\mu} \in \mathbb{R}^d$, $\gamma^{(1)}, \dots, \gamma^{(d)}, \beta \in \mathbb{R}^+$ are learnable parameters. By setting all the other modules and the interpolation neighborhood sizes as the same, we compare performance on different meshes of the two interpolation kernels in Table. 3 (Gaus + LN), where the adaptively learned kernels achieve better accuracy.

Benefits from normalization layers. Previous works demonstrated the normalization is necessary for network architecture, for fast convergence and stable training (Dong et al., 2021; Ba et al., 2016). A notable difference between NFS and FNO is that the Layer-Norm can be implemented in NFS's layers without disabling its discretization-invariance. The improvements brought from the normalization layers are given in Table. 3 (Flex + ~~LN~~), where the performance gap is obvious on unseen meshes.

4.4 Non-equispaced Vision Mixers

Since NFS can be regarded as a combination of our interpolation layers with the revised FNO, our interpolation layers can also be implemented in the other Vision Mixers, so that these methods are equipped with the ability to handle non-equispaced data. Details are given in Appendix. B.7. We find that *(1)* From Table. B10 and Table. 1, the degeneration of performance is obvious in other Vision Mixers. In comparison, FNO as intermediate equispaced layers, truncates the high frequency in its channel mixing and retains the low frequency shared by both resampled and original signals, so the loss of accuracy in non-equispaced scenarios is tiny in our NFS; *(2)* Although the performance on unseen meshes is more stable in these non-equispaced Vision Mixers, the performance gap is still large, according to Table. B10 and Table. 3.

4.5 Complexity comparison

The discussed Fig. 2 shows time complexity of each method. Vision Mixers are the fastest, while graph spatio-temporal models are far much slower. NFS falls in between because the interpolation layer can be an analogy to a graph-message-passing layer (See Sec. 3.3), and the intermediate are equispaced token-channel mixing layers of Vision Mixers' structure. Memory usage shows storing each point's neighbors in the interpolation layer is very memory-consuming.

5 Conclusion and Future Work

A simple method called NFS is established based on FNO, with theoretically enough expressiveness, allowing non-equispaced scenarios and fast computation for solving PDEs, and achieves state-of-the-art performance in equispaced and non-equispaced scenarios. Problems still exist, including **relatively high error on unseen meshes** and **high memory cost in the interpolation layers**.

REFERENCES

James Atwood and Don Towsley. Diffusion-convolutional neural networks, 2016.

Jimmy Lei Ba, Jamie Ryan Kiros, and Geoffrey E. Hinton. Layer normalization, 2016. URL https://arxiv.org/abs/1607.06450.

Lei Bai, Lina Yao, Can Li, Xianzhi Wang, and Can Wang. Adaptive graph convolutional recurrent network for traffic forecasting, 2020.

Leah Bar and Nir Sochen. Unsupervised deep learning algorithm for pde-based forward and inverse problems, 2019.

Saakaar Bhatnagar, Yaser Afshar, Shaowu Pan, Karthik Duraisamy, and Shailendra Kaushik. Prediction of aerodynamic flow fields using convolutional neural networks. *Computational Mechanics*, 64(2):525–545, jun 2019. doi: 10.1007/s00466-019-01740-0. URL https://doi.org/10.1007%2Fs00466-019-01740-0.

Kaushik Bhattacharya, Bamdad Hosseini, Nikola B. Kovachki, and Andrew M. Stuart. Model reduction and neural networks for parametric pdes, 2021.

Johannes Brandstetter, Daniel Worrall, and Max Welling. Message passing neural pde solvers, 2022. URL https://arxiv.org/abs/2202.03376.

Umer I. Cheema, Gregory Nash, Rashid Ansari, and Ashfaq Khokhar. Memory-optimized re-gridding architecture for non-uniform fast fourier transform. *IEEE Transactions on Circuits and Systems I: Regular Papers*, 64(7):1853–1864, 2017. doi: 10.1109/TCSI.2017.2681723.

Ricky T. Q. Chen, Yulia Rubanova, Jesse Bettencourt, and David Duvenaud. Neural ordinary differential equations, 2019.

Tianping Chen and Hong Chen. Universal approximation to nonlinear operators by neural networks with arbitrary activation functions and its application to dynamical systems. *IEEE Transactions on Neural Networks*, 6(4):911–917, 1995. doi: 10.1109/72.392253.

Xiangxiang Chu, Zhi Tian, Yuqing Wang, Bo Zhang, Haibing Ren, Xiaolin Wei, Huaxia Xia, and Chunhua Shen. Twins: Revisiting the design of spatial attention in vision transformers, 2021. URL https://arxiv.org/abs/2104.13840.

Michaël Defferrard, Xavier Bresson, and Pierre Vandergheynst. Convolutional neural networks on graphs with fast localized spectral filtering, 2017.

Yihe Dong, Jean-Baptiste Cordonnier, and Andreas Loukas. Attention is not all you need: Pure attention loses rank doubly exponentially with depth, 2021. URL https://arxiv.org/abs/2103.03404.

Alexey Dosovitskiy, Lucas Beyer, Alexander Kolesnikov, Dirk Weissenborn, Xiaohua Zhai, Thomas Unterthiner, Mostafa Dehghani, Matthias Minderer, Georg Heigold, Sylvain Gelly, Jakob Uszkoreit, and Neil Houlsby. An image is worth 16x16 words: Transformers for image recognition at scale, 2020. URL https://arxiv.org/abs/2010.11929.

A. Dutt and V. Rokhlin. Fast fourier transforms for nonequispaced data, ii. *Applied and Computational Harmonic Analysis*, 2(1):85–100, 1995. ISSN 1063-5203. doi: https://doi.org/10.1006/acha.1995.1007. URL https://www.sciencedirect.com/science/article/pii/S106352038571007X.

Weinan E and Bing Yu. The deep ritz method: A deep learning-based numerical algorithm for solving variational problems, 2017.

Justin Gilmer, Samuel S. Schoenholz, Patrick F. Riley, Oriol Vinyals, and George E. Dahl. Neural message passing for quantum chemistry, 2017.

John Guibas, Morteza Mardani, Zongyi Li, Andrew Tao, Anima Anandkumar, and Bryan Catanzaro. Adaptive fourier neural operators: Efficient token mixers for transformers, 2021. URL https://arxiv.org/abs/2111.13587.

Xiaoxiao Guo, Wei Li, and Francesco Iorio. Convolutional neural networks for steady flow approximation. In *Proceedings of the 22nd ACM SIGKDD International Conference on Knowledge Discovery and Data Mining*, KDD '16, pp. 481–490, New York, NY, USA, 2016. Association for Computing Machinery. ISBN 9781450342322. doi: 10.1145/2939672.2939738. URL https://doi.org/10.1145/2939672.2939738.

Kurt Hornik, Maxwell Stinchcombe, and Halbert White. Multilayer feedforward networks are universal approximators. *Neural Networks*, 2(5):359–366, 1989. ISSN 0893-6080. doi: https://doi.org/10.1016/0893-6080(89)90020-8. URL https://www.sciencedirect.com/science/article/pii/0893608089900208.

Valerii Iakovlev, Markus Heinonen, and Harri Lähdesmäki. Learning continuous-time pdes from sparse data with graph neural networks, 2020. URL https://arxiv.org/abs/2006.08956.

Dhiraj D. Kalamkar, Joshua D. Trzaskoz, Srinivas Sridharan, Mikhail Smelyanskiy, Daehyun Kim, Armando Manduca, Yunhong Shu, Matt A. Bernstein, Bharat Kaul, and Pradeep Dubey. High performance non-uniform fft on modern x86-based multi-core systems. In *2012 IEEE 26th International Parallel and Distributed Processing Symposium*, pp. 449–460, 2012. doi: 10.1109/IPDPS.2012.49.

Srinidhi Kestur, Sungho Park, Kevin M. Irick, and Vijaykrishnan Narayanan. Accelerating the nonuniform fast fourier transform using fpgas. In *2010 18th IEEE Annual International Symposium on Field-Programmable Custom Computing Machines*, pp. 19–26, 2010. doi: 10.1109/FCCM.2010.13.

YUEHAW KHOO, JIANFENG LU, and LEXING YING. Solving parametric PDE problems with artificial neural networks. *European Journal of Applied Mathematics*, 32(3):421–435, jul 2020. doi: 10.1017/s0956792520000182. URL https://doi.org/10.1017%2Fs0956792520000182.

Nikola Kovachki, Zongyi Li, Burigede Liu, Kamyar Azizzadenesheli, Kaushik Bhattacharya, Andrew Stuart, and Anima Anandkumar. Neural operator: Learning maps between function spaces, 2021. URL http://tensorlab.cms.caltech.edu/users/anima/pubs/GraphPDE_Journal.pdf.

Yaguang Li, Rose Yu, Cyrus Shahabi, and Yan Liu. Diffusion convolutional recurrent neural network: Data-driven traffic forecasting, 2018.

Zongyi Li, Nikola Kovachki, Kamyar Azizzadenesheli, Burigede Liu, Kaushik Bhattacharya, Andrew Stuart, and Anima Anandkumar. Neural operator: Graph kernel network for partial differential equations, 2020a. URL https://arxiv.org/abs/2003.03485.

Zongyi Li, Nikola Kovachki, Kamyar Azizzadenesheli, Burigede Liu, Kaushik Bhattacharya, Andrew Stuart, and Anima Anandkumar. Multipole graph neural operator for parametric partial differential equations, 2020b.

Zongyi Li, Nikola Kovachki, Kamyar Azizzadenesheli, Burigede Liu, Kaushik Bhattacharya, Andrew Stuart, and Anima Anandkumar. Fourier neural operator for parametric partial differential equations, 2020c. URL https://arxiv.org/abs/2010.08895.

Haitao Lin, Zhangyang Gao, Yongjie Xu, Lirong Wu, Ling Li, and Stan. Z. Li. Conditional local convolution for spatio-temporal meteorological forecasting, 2021.

Haitao Lin, Guojiang Zhao, Lirong Wu, and Stan Z. Li. Stonet: A neural-operator-driven spatio-temporal network, 2022. URL https://arxiv.org/abs/2204.08414.

Ze Liu, Yutong Lin, Yue Cao, Han Hu, Yixuan Wei, Zheng Zhang, Stephen Lin, and Baining Guo. Swin transformer: Hierarchical vision transformer using shifted windows, 2021. URL https://arxiv.org/abs/2103.14030.

Lu Lu, Pengzhan Jin, Guofei Pang, Zhongqiang Zhang, and George Em Karniadakis. Learning nonlinear operators via deeponet based on the universal approximation theorem of operators. *Nature Machine Intelligence*, 3:218–229, 2021.

Xiaofeng Mao, Gege Qi, Yuefeng Chen, Xiaodan Li, Ranjie Duan, Shaokai Ye, Yuan He, and Hui Xue. Towards robust vision transformer, 2021. URL https://arxiv.org/abs/2105.07926.

Muzammal Naseer, Kanchana Ranasinghe, Salman Khan, Munawar Hayat, Fahad Shahbaz Khan, and Ming-Hsuan Yang. Intriguing properties of vision transformers, 2021. URL https://arxiv.org/abs/2105.10497.

Nicholas H. Nelsen and Andrew M. Stuart. The random feature model for input-output maps between banach spaces, 2021.

Shaowu Pan and Karthik Duraisamy. Physics-informed probabilistic learning of linear embeddings of nonlinear dynamics with guaranteed stability. *SIAM Journal on Applied Dynamical Systems*, 19 (1):480–509, Jan 2020. ISSN 1536-0040. doi: 10.1137/19m1267246. URL http://dx.doi.org/10.1137/19M1267246.

Namuk Park and Songkuk Kim. How do vision transformers work?, 2022. URL https://arxiv.org/abs/2202.06709.

C. Rader and N. Brenner. A new principle for fast fourier transformation. *IEEE Transactions on Acoustics, Speech, and Signal Processing*, 24(3):264–266, 1976. doi: 10.1109/TASSP.1976.1162805.

Maziar Raissi, Alireza Yazdani, and George Em Karniadakis. Hidden fluid mechanics: Learning velocity and pressure fields from flow visualizations. *Science*, 367(6481):1026–1030, 2020.

Yongming Rao, Wenliang Zhao, Zheng Zhu, Jiwen Lu, and Jie Zhou. Global filter networks for image classification, 2021. URL https://arxiv.org/abs/2107.00645.

Yulia Rubanova, Ricky T. Q. Chen, and David Duvenaud. Latent odes for irregularly-sampled time series, 2019.

Youngjoo Seo, Michaël Defferrard, Pierre Vandergheynst, and Xavier Bresson. Structured sequence modeling with graph convolutional recurrent networks, 2016.

Justin Sirignano and Konstantinos Spiliopoulos. DGM: A deep learning algorithm for solving partial differential equations. *Journal of Computational Physics*, 375:1339–1364, dec 2018. doi: 10.1016/j.jcp.2018.08.029. URL https://doi.org/10.1016%2Fj.jcp.2018.08.029.

Jonathan D. Smith, Kamyar Azizzadenesheli, and Zachary E. Ross. Eikonet: Solving the eikonal equation with deep neural networks, 2020.

Ilya Tolstikhin, Neil Houlsby, Alexander Kolesnikov, Lucas Beyer, Xiaohua Zhai, Thomas Unterthiner, Jessica Yung, Andreas Steiner, Daniel Keysers, Jakob Uszkoreit, Mario Lucic, and Alexey Dosovitskiy. Mlp-mixer: An all-mlp architecture for vision, 2021. URL https://arxiv.org/abs/2105.01601.

Shikhar Tuli, Ishita Dasgupta, Erin Grant, and Thomas L. Griffiths. Are convolutional neural networks or transformers more like human vision?, 2021. URL https://arxiv.org/abs/2105.07197.

Matthew A. Wright and Joseph E. Gonzalez. Transformers are deep infinite-dimensional non-mercer binary kernel machines, 2021. URL https://arxiv.org/abs/2106.01506.

Baosong Yang, Longyue Wang, Derek Wong, Lidia S. Chao, and Zhaopeng Tu. Convolutional self-attention networks, 2019. URL https://arxiv.org/abs/1904.03107.

Çağatay Yıldız, Markus Heinonen, and Harri Lähdesmäki. Ode^{2}vae: Deep generative second order odes with bayesian neural networks, 2019.

A METHODS

A.1 NOTATION

Symbol	Used for
$\boldsymbol{X}$	A discretization of the domain D, which is used to train the model.
$\boldsymbol{X'}$	A discretization of the domain D, which is used to evaluate the model.
$\boldsymbol{x}$	Coordinate of spatial point in D.
n_s	Number of spatial points of seen meshes for training, as $\lvert\boldsymbol{X}\rvert = n_s$.
n'_s	Number of spatial points of unseen meshes for inference, as $\lvert\boldsymbol{X'}\rvert = n'_s$.
n_t	Number of input timestamps as the number of input time-dependent PDE's initial states.
n'_t	Number of output timestamps as the number of output time-dependent PDE's future states.
a	Input function, where $a \in \mathcal{A}(D; \mathbb{R}^{d_a})$ means for $\boldsymbol{x} \in D$, $a(\boldsymbol{x}) \in \mathbb{R}^{d_a}$. In time-dependent PDEs, $a = u(\cdot, \boldsymbol{T})$, where $\boldsymbol{T} = \{t_i\}_{i=1}^{n_t}$.
u	Target function for approximation, where $u \in \mathcal{U}(D; \mathbb{R}^{d_u})$ means for $\boldsymbol{x} \in D$, $u(\boldsymbol{x}) \in \mathbb{R}^{d_u}$.
v	Representation function, where $v \in \mathcal{U}(D; \mathbb{R}^{d_v})$ means for $\boldsymbol{x} \in D$, $v(\boldsymbol{x}) \in \mathbb{R}^{d_v}$, which is a function obtained by a lifter which project a into a higher dimensional space.
$\mathcal{G}_\theta$	Approximation operator, where $\mathcal{G}_\theta(a) \approx u$.
μ	The probability measure for sampling Spatial points $\boldsymbol{x}$, which is supported on D.
$\mathcal{C}$	Cost functional as the minimum optimization target.
$\mathcal{F}$	Discrete Fourier transform for equispaced spatial points.
$\mathcal{F}^{-1}$	Discrete Inverse Fourier transform for equispaced spatial points.
P	Project operator, with $P(a)(\boldsymbol{x}) \in \mathbb{R}^{d_v}$.
Q	Project operator, with $Q(v)(\boldsymbol{x}) \in \mathbb{R}^{d_u}$.
v^{t}	t-th iterative representation function after kernel operators' update.
$\mathcal{K}_\phi$	Kernel integral operator mapping, which maps a to a bounded linear operator, with parameter ϕ.
W	Linear transform on the d_v dimension (channel) of $v(\boldsymbol{x}) \in d_v$.
R_ϕ	Fourier transform of a periodic kernel function, which is learnable parameters in a single iterative process in FNO.
ChannelMix	Channel-mixing operator as a linear transform in the dimensoion of channel (d_v).
TokenMix	Token-mixing operator as a linear transform in the dimensoion of spatial points (n_s).
$\tilde{\mathcal{F}}$	Proposed non-equispaced Fourier transform, where $\tilde{\mathcal{F}} = (\mathcal{F} \circ \mathcal{H}(a))$.
m_s	Spatial points' number on resampled equi-spaced points.
$\mathcal{H}$	Interpolation operator to interpolate the non-equispaced spatial points on equispaced spatial grids.
τ	Parameter in Gaussian interpolation kernels controlling smoothness of the kernel.
$\boldsymbol{\mu}$	Parameter in Gaussian interpolation kernels, as the mean of Gaussian kernels.
$\mathcal{H}_\eta$	Interpolation operator mapping, where $\mathcal{H}_\eta(a)$ is an interpolation operator used to map signals on the non-equispaced spatial points to equispaced spatial grids.
$\mathcal{H}'_\zeta$	Interpolation operator mapping, where $\mathcal{H}'_\zeta(a)$ is a interpolation operator used to map signals on the equispaced spatial points to non-equispaced spatial grids.
$\mathcal{N}(\boldsymbol{x})$	Neighborhood of spatial point $\boldsymbol{x}$.

Table A1: Glossary of Notations used in this paper.

A.2 GRAPH CONSTRUCTION

Neighborhood construction. Instead of using K-nearest neighborhood method, the neighborhood system in the interpolation layer is constructed by ϵ-ball, because in equispace scenarios, there will be multiple points as K-th nearest neighbor at the same time. For point $\boldsymbol{x}$, its neighbor is defined according to

$$\begin{cases} d(\boldsymbol{x}, \boldsymbol{x}_i) \leq \epsilon & \boldsymbol{x}_i \in \mathcal{N}(\boldsymbol{x}); \\ d(\boldsymbol{x}, \boldsymbol{x}_i) > \epsilon & \boldsymbol{x}_i \notin \mathcal{N}(\boldsymbol{x}). \end{cases} \tag{11}$$

For given c defined in Sec. 3.2, we can restrict ϵ so that $\mathbb{E}_{x\sim\mu}[|\mathcal{N}(\boldsymbol{x})|] < c\log(n_s)$.

A.3 PROOF OF THEOREM 3.1.

Our proof is mostly based on Chen & Chen (1995) and Kovachki et al. (2021). For notation simplicity, in the proof, we directly write $\mathcal{H}_\eta(a)$ as $\mathcal{H}_\eta$ as the linear operator.

Lemma A1. *Let $\mathcal{X}$ be a Banach space, and $\mathcal{U} \subseteq \mathcal{X}$ a compact set, and $\mathcal{K} \subset \mathcal{X}$ a dense set. Then, for any $\epsilon > 0$, there exists a number $n \in \mathbb{N}$, and a series of continuous, linear functionals $G_1, G_2, \ldots, G_n \in C(\mathcal{U}; \mathbb{R})$, and elements $\varphi_1, \ldots, \varphi_n \in \mathcal{K}$, such that*

$$\sup_{u\in\mathcal{U}} ||v - \sum_{j=1}^{n} G_j(v)\varphi_j||_{\mathcal{X}} \leq \epsilon \tag{12}$$

The proof is given in **Lemma 7.** in Kovachki et al. (2021), and **Theorem 3.** and **4.** for reference .

Theorem A2. *Let $D \subseteq \mathbb{R}^d$ be compact domain. Let $\mathcal{U}$ be a separable Banach space of real-valued functions on D, such that $C(D, \mathbb{R}) \subseteq \mathcal{U}$ is dense. Suppose $\mathcal{U} = L^p(D; \mathbb{R})$ for any $1 < p < \infty$. ν is a probability measure supported on $\mathcal{U}$ and assume that, $\mathbb{E}_{v\sim\nu}||v||_{\mathcal{U}} < \infty$ for any $v \in \mathcal{U}$. μ is a probabilistic measure supported on D, which defines the inner product of Hilbert space $\mathcal{U}$ as $< f, g >_{\mathcal{U}} = \int_D f(\boldsymbol{x})g(\boldsymbol{x})d\mu(\boldsymbol{x})$. Then, there exists a neural network $h_\eta : \mathbb{R}^d \times \mathbb{R}^d \to \mathbb{R}$ whose activation functions are of the Tauber-Wiener class, such that*

$$||v - \mathcal{H}(v)||_{\mathcal{U}} \leq \epsilon,$$

where $\mathcal{H}(v)(\boldsymbol{x}) = \int_D h_\eta(\boldsymbol{x}, \boldsymbol{y})v(\boldsymbol{y})d\mu(\boldsymbol{y})$.

Proof. Since $\mathcal{U}$ is a Polish space, we can find a compact set $\mathcal{K}$, such that $\nu(\mathcal{U} \setminus \mathcal{K}) \leq \epsilon$. Therefore, **Lemma A1** can be applied, to find a number $n \in \mathbb{N}$, a series of continuous linear functionals $G_j \in C(\mathcal{U}; \mathbb{R})$ and functions $\varphi_j \in C(D; \mathbb{R})$ such that

$$\sup_{v\in\mathcal{K}} ||v - \sum_{j=1}^{n} G_j(v)\varphi_j||_{\mathcal{U}} \leq \epsilon.$$

Denote $\hat{\mathcal{H}}_n(v) = \sum_{j=1}^{n} G_j(v)\varphi_j$, and let $1 < q < \infty$ be the Hölder conjugate of p. Since $\mathcal{U} = L^p(D; \mathbb{R})$, by Reisz Representation Theorem, there exists functions $g_j \in L^q(D; \mathbb{R})$, such that $G_j(v) = \int_D v(\boldsymbol{x})g_j(\boldsymbol{x})d\mu(\boldsymbol{x})$ for $j = 1, \ldots, n$ and $v \in L^p(D; \mathbb{R})$. By density of $C(D; \mathbb{R})$ in $L^q(D; \mathbb{R})$, we can find functions $\psi_1, \ldots, \psi_n \in C(D; \mathbb{R})$, such that

$$\sup_{j\in\{1,\ldots,n\}} ||\psi_j - g_j||_{L^q(D;\mathbb{R})} \leq \epsilon/n.$$

Then, we define $\tilde{\mathcal{H}}_n : L^p(D; \mathbb{R}) \to C(D; \mathbb{R})$ by

$$\tilde{\mathcal{H}}_n(v) = \sum_{j=1}^{n} \int_D \psi_j(\boldsymbol{y})v(\boldsymbol{y})d\mu(\boldsymbol{y})\varphi_j(\boldsymbol{x}).$$

For the universal approximation (density) (Hornik et al., 1989) of neural networks, we can find a Multi-layer Feedforward network $h_\eta : \mathbb{R}^d \times \mathbb{R}^d \to \mathbb{R}$ whose activation functions are of the Tauber-Wiener class, such that

$$\sup_{\boldsymbol{x},\boldsymbol{y}\in D} |h_\eta(\boldsymbol{x}, \boldsymbol{y}) - \sum_{j=1}^{n} \psi_j(\boldsymbol{y})\varphi_j(\boldsymbol{x})| \leq \epsilon.$$

Let $\mathcal{H}_\eta(\boldsymbol{x}) = \int_D h_\eta(\boldsymbol{x}, \boldsymbol{y}) v(\boldsymbol{y}) d\mu(\boldsymbol{y})$. Then, there exists a constant $C_1 > 0$, such that

$$||\hat{\mathcal{H}}_n(v) - \mathcal{H}(v)||_{L^p(D;\mathbb{R})} \leq C_1(||\hat{\mathcal{H}}_n(v) - \tilde{\mathcal{H}}_n(v)||_{L^p(D;\mathbb{R})} + ||\tilde{\mathcal{H}}_n(v) - \mathcal{H}(v)||_{L^p(D;\mathbb{R})}).$$

For the first term, there is a constant $C_2 > 0$, such that

$$\begin{aligned}
||\hat{\mathcal{H}}_n(v) - \tilde{\mathcal{H}}_n(v)||_{L^p(D;\mathbb{R})} &\leq C_2 \sum_{j=1}^{n} || \int_D v(\boldsymbol{y})(g_j(\boldsymbol{y}) - \psi_j(\boldsymbol{y})) d\mu(\boldsymbol{y}) \varphi_j||_{L^p(D;\mathbb{R})} \\
&\leq C_2 \sum_{j=1}^{n} ||v(\boldsymbol{y})||_{L^p(D;\mathbb{R})} ||g_j(\boldsymbol{y}) - \psi_j(\boldsymbol{y})||_{L^q(D;\mathbb{R})} ||\varphi_j||_{L^p(D;\mathbb{R})} \\
&\leq C_3 \epsilon ||v(\boldsymbol{y})||_{L^p(D;\mathbb{R})},
\end{aligned}$$

for some $C_3 > 0$. And for the second term,

$$\begin{aligned}
||\tilde{\mathcal{H}}_n(v) - \mathcal{H}(v)||_{L^p(D;\mathbb{R})} &= || \int_D v(\boldsymbol{y})(\sum_{j=1}^{n} \psi_j(\boldsymbol{y}) \varphi_j(\cdot) - h_\eta(\cdot, \boldsymbol{y})) d\mu(\boldsymbol{y})||_{L^p(D;\mathbb{R})} \\
&\leq |D| \epsilon ||v||_{L^p(D;\mathbb{R})},
\end{aligned}$$

Therefore, there is a constant $C > 0$, such that

$$\int_{\mathcal{U}} ||\hat{\mathcal{H}}_n(v) - \tilde{\mathcal{H}}_n(v)||_{\mathcal{U}} d\nu(v) \leq \epsilon C \mathbb{E}_{v \sim \nu} ||v||_{\mathcal{U}}$$

. Because of the assumption that $\mathbb{E}_{v \sim \nu} ||v||_{\mathcal{U}} < \infty$, and ϵ is arbitrary, then

$$||v - \mathcal{H}(v)||_{\mathcal{U}} \leq ||v - \hat{\mathcal{H}}_n(v)||_{\mathcal{U}} + ||\hat{\mathcal{H}}_n(v) - \mathcal{H}(v)||_{\mathcal{U}},$$

the proof is complete. □

Corollary A3. *Define $\mathcal{H}_\eta(v) = \int_D h_\eta(\boldsymbol{x} - \boldsymbol{y}, \boldsymbol{x}, a(\boldsymbol{y})) v(\boldsymbol{y}) d\mu(\boldsymbol{y})$, the interpolation operator can also approximate v to any precision ϵ.*

Proof. We use a one-layer neural network $h_\eta : D \times D \to \mathbb{R}$ as an example, which is defined as $h_\eta(\boldsymbol{x}, \boldsymbol{y}, a(\boldsymbol{y}) = \sigma(\sum_{i=1}^{d} w_{x,i} x^{(i)} + w_{y,i} y^{(i)} + b)$. We can rewrite it as

$$h_\eta = \sigma(\sum_{i=1}^{d} w_{x,i}(x^{(i)} - y^{(i)}) + (w_{y,i} + w_{x,i}) y^{(i)} + \sum_{j=1}^{d_a} w_{a,j} a^{(j)}(\boldsymbol{y}) + b),$$

where $w_{a,j} = 0$. □

Corollary A4. *The **Theorem A2** and **Corollary A3** can be extended for $v : D \to \mathbb{R}^{d_v}$, where $d_v > 1$.*

Proof. As $v = (v^{(1)}, v^{(2)}, \ldots, v^{(d_v)})$, for each $v^{(j)}$, a single neural network can be used for approximation. Moreover, in implementation, we make h_η fully-connected, to improve the expressivity. □

Remark. *As $\sum_{\boldsymbol{x}_i \in \boldsymbol{X}} v(\boldsymbol{x}_i) h_\eta(\boldsymbol{x} - \boldsymbol{x}_i, \boldsymbol{x}_i, a(\boldsymbol{x}_i))$ is the unbiased estimation of $\mathbb{E}_{\boldsymbol{y} \sim \mu}(h_\eta(\boldsymbol{x}, \boldsymbol{y}) v(\boldsymbol{y}))$, we use the Equation. (8) for the approximation.*

B EXPERIMENTS

B.1 BENCHMARK METHOD DESCRIPTION

Vision Mixers. We provide a framework for vision mixers as PDE solvers, including VIT, MLP-MIXER, FNET, GFN, FNO, PFNO and our NFS. The intermediate architecture of mixing layers is shown in Fig. B1. The code of our framework will be released soon. And the resampling and back-sampling methods are stacked before 'Equispaced Input' and 'Equispaced Output'. In this way, the description of the Vision Mixers included in our framework can be described by different modules, as shown in Table. B1. All the trials on Vision Mixers set *embedding size* as 32, *batch size* as 4, *layer number* of the intermediate equispaced mixing layers as 2. In FNO and PFNO, the truncated $K_{\max}$ is set as 16. The *patch size* of Vision Mixers with patchwise embedding are set as $[4, 2]$ in 1-d PDEs and $[4, 4, 2]$ in 2-d PDEs. The interpolation layers in NFS are composed of one layer of feed-forward network whose perceptron unit is equal to $4\times$ *embedding size* of the model.

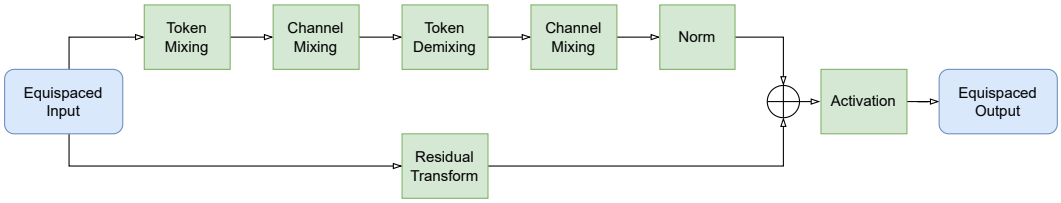

Figure B1: The architecture of Vision Mixers.

Table B1: Description of Vison Mixers in the unifying framework module by module.

Modules	VIT	MLPMIXER	FNET	GFN	FNO	PFNO	NFS
Resampling	Patchwise Embedding	Patchwise Embedding	Patchwise Embedding	Patchwise Embedding	Identity	Patchwise Embedding	Interpolation
Token Mixing	Attention	MLP	Fourier	Fourier	Fourier	Fourier	Fourier
Channel Mixing	Linear	Linear	Linear	Elementwise Product	Low Frequency MatMultiply	Low Frequency MatMultiply	Low Frequency MatMultiply
Token Demixing	Identity	Identity	Identity	Inverse Fourier	Inverse Fourier	Inverse Fourier	Inverse Fourier
Channel Mixing	Identity	Identity	Identity	Linear	Identity	Identity	Identity
Normalization	LayerNorm	LayerNorm	Complex LayerNorm	LayerNorm	Identity	LayerNorm	LayerNorm
Residual	Identity	Identity	Identity	Identity	1x1 Conv	1x1 Conv	1x1 Conv
Activation	Gelu	Gelu	Complex Gelu	Gelu	Gelu	Gelu	Gelu
Back Sampling	Linear+ Rearrange	Linear+ Rearrange	Linear+ Rearrange	Linear+ Rearrange	Identity	Linear+ Rearrange	Interpolation

Graph Spatio-Temporal Models. The evaluated graph spatio-temporal neural networks are based on recurrent neural networks for dynamics modeling, where the spatial dependency is modeled by graph neural networks. The spatial and temporal modules for AGCRN, DCRNN and GCGRU are shown in Table. B2. MPPDE used different architecture, with the pushforward trick used for taining, with *rolling* equaling 1 and *time window* equaling to 10 . All the trials on these graph spatio-tempral models set *embedding size* as 64, except MPPDE as 128. *Batch size* is set as 4. When the graph convolution needs multi-hop message-passing, we set the hop as 2. For MPPDE, the layer number of GNNs is 6. The *embedding dimension* in AGCRN is set as 2.

Table B2: Description of different graph spatio-temporal models

Methods	Spatial module	Temporal module
GCGRU Seo et al. (2016)	Cheb Conv Defferrard et al. (2017)	GRU
DCRNN Li et al. (2018)	Diff Conv Atwood & Towsley (2016)	GRU
AGCRN Bai et al. (2020)	Node Similarity Bai et al. (2020)	GRU

B.2 DATA GENERATION

Burgers' Equation. The initial condition $u_0(x)$ is generated according to $u_0 \sim N(0.625(-\Delta + 25I)^{-2})$ with periodic boundary conditions. ν is set as 0.01. $x \in [0, 1]$ and $t \in [0, 1]$. The spatial resolution is 1024, and time resolution is 200. The dataset generation follows FNO's protocol, which can be downloaded from its source code on official Github.

KdV Equation. The equation is written as

$$\partial_t u(x,t) + 3\partial_x u^2(x,t) + \partial_x^3 u(x,t) = 0, \tag{13}$$

where $x \in [0, 1]$. The initial condition $u_0(x)$ is calculated as

$$u(x, 0) = \sum_{i=1}^{K} 0.5 c_i \cos(0.5\sqrt{c_i + b_i} x - a_i)$$

where $c_i \sim N(0, \sigma_i)$, and $a_i, b_i > 0$. The spatial resolution is 1024. The dataset is generated by `scipy` package, with `fftpack.diff` used as pesudo-differential method and `odeint` used as forward Euler method.

Darcy Flow. The equation is written as

$$\begin{aligned} -\nabla(a(\boldsymbol{x})\nabla u(\boldsymbol{x})) &= f(\boldsymbol{x}) & \boldsymbol{x} &\in (0,1)^2 \\ u(\boldsymbol{x}) &= 0 & \boldsymbol{x} &\in \partial[0,1]^2 \end{aligned} \tag{14}$$

The original resolution is 256×256. $a(\boldsymbol{x})$ is generated by Gaussian random field, and we directly establish the operator to learn the mapping of a to u.

NS Equation. Our generation of NS Equation is based on FNO's Appendix. A.3.3, with the forcing is kept fixed. The original spatial resolution is 128×128, and time resolution is 200.

B.3 Complete Results on Model Comparison

Here we give complete results on the four Equations. Table. B3 give the performance comparison on Darcy flow of both equispaced and non-equispaced scenarios. Table. B4 and B5 gives performance comparison in equispaced scenarios on the other three time-dependent problems. Table. B6 and B7 gives performance comparison in non-equispaced scenarios on the other three time-dependent problems. In all the tasks except `Darcy Flow`, the depth of layer is set as 2, and $k_{\max} = 16$ in both NFS and FNO. However, we find in `Darcy Flow`, $k_{\max}$ should be set much larger, or the loss will not decrease. In the reported results, $k_{\max} = 32, 64, 128$ in `Darcy Flow`.

Table B3: Performance comparison on Darcy Flow.

	MAE ($\times 10^{-3}$)	RMSE($\times 10^{-3}$)	MAE($\times 10^{-3}$)	RMSE($\times 10^{-3}$)	MAE($\times 10^{-3}$)	RMSE($\times 10^{-3}$)
	`Darcy Flow` ($r = 64$)		`Darcy Flow` ($r = 128$)		`Darcy Flow` ($r = 256$)	
VIT	0.5073$_{\pm 0.0411}$	0.8468$_{\pm 0.0432}$	0.9865$_{\pm 0.0002}$	1.6195$_{\pm 0.0007}$	1.1078$_{\pm 0.0021}$	1.8444$_{\pm 0.0023}$
MLPMixer	0.4970$_{\pm 0.0021}$	0.8228$_{\pm 0.0034}$	0.8909$_{\pm 0.0099}$	1.4221$_{\pm 0.0118}$	0.9125$_{\pm 0.0024}$	1.6459$_{\pm 0.0032}$
GFN	0.4739$_{\pm 0.0016}$	0.8345$_{\pm 0.0019}$	0.8659$_{\pm 0.0046}$	1.4237$_{\pm 0.0071}$	0.9618$_{\pm 0.0124}$	1.6139$_{\pm 0.0128}$
FNO	0.4289$_{\pm 0.0051}$	0.7740$_{\pm 0.0046}$	0.7086$_{\pm 0.0045}$	0.1324$_{\pm 0.0019}$	0.9075$_{\pm 0.0051}$	1.4940$_{\pm 0.0046}$
NFS	**0.1497**$_{\pm 0.0005}$	**0.1962**$_{\pm 0.0007}$	**0.2254**$_{\pm 0.0007}$	**0.7245**$_{\pm 0.0009}$	**0.4216**$_{\pm 0.0033}$	**0.8578**$_{\pm 0.0041}$
	`Darcy Flow` ($n_s = 1024$)		`Darcy Flow` ($n_s = 4096$)		`Darcy Flow` ($n_s = 16384$)	
DCRNN	1.8146$_{\pm 0.0060}$	2.6352$_{\pm 0.0029}$	1.7629$_{\pm 0.0003}$	2.5760$_{\pm 0.0001}$	OOM	OOM
AGCRN	1.6938$_{\pm 0.0001}$	2.4440$_{\pm 0.0001}$	1.7336$_{\pm 0.0001}$	2.4167$_{\pm 0.0001}$	OOM	OOM
GCGRU	1.7633$_{\pm 0.0001}$	2.5696$_{\pm 0.0001}$	1.7403$_{\pm 0.0001}$	2.5363$_{\pm 0.0001}$	OOM	OOM
MPPDE	0.6673$_{\pm 0.0009}$	0.9290$_{\pm 0.0012}$	0.5608$_{\pm 0.0053}$	0.8424$_{\pm 0.0051}$	0.6384$_{\pm 0.0005}$	0.8748$_{\pm 0.0005}$
NFS	**0.1727**$_{\pm 0.0047}$	**0.2311**$_{\pm 0.0066}$	**0.1430**$_{\pm 0.0007}$	**0.1914**$_{\pm 0.0014}$	**0.2379**$_{\pm 0.0007}$	**0.3489**$_{\pm 0.0009}$

NFS fails to model the non-equispaced Burgers' Equation when n_t is set as 1, in which the performance is far from it can achieve in equispaced scenarios. Such problem will be our future work.

Table B4: Performance comparison with Vision Mixer benchmarks on different equations ($n_t = 1$). Validation loss on `Burgers'` ($n_t = 1$) of VIT, GFN, and FNO does not converge. The results show that the early-stopping occurs in the begining of training.

Vision Mixers	MAE ($\times 10^{-3}$)	RMSE($\times 10^{-3}$)	MAE($\times 10^{-3}$)	RMSE($\times 10^{-3}$)	MAE($\times 10^{-3}$)	RMSE($\times 10^{-3}$)
	`Burgers'` ($r = 512, n_t' = 10$)		`Burgers'` ($r = 512, n_t' = 40$)		`Burgers'` ($r = 1024, n_t' = 20$)	
VIT	201.6539±0.5284	231.9138±0.8403	183.6696±0.3015	210.6237±0.6767	195.5858±0.7706	224.4712±1.2472
MLPMixer	201.6547±0.0671	231.9163±0.0263	183.6535±0.0599	210.6160±0.0305	195.5960±0.0240	224.4791±0.0132
GFN	201.6557±0.9513	231.9122±0.9535	183.6674±0.4893	210.6165±0.4831	195.5918±0.0471	224.4736±0.0681
FNO	201.6527±1.1415	231.9119±1.6747	183.6696±0.3015	210.6299±0.4983	195.5902±0.9304	224.4723±0.9230
NFS	**0.1806**±0.0005	**0.2669**±0.0010	**0.3570**±0.0008	**0.5340**±0.0009	**0.4344**±0.0014	**0.6092**±0.0017
	`KdV` ($r = 512, n_t' = 10$)		`KdV` ($r = 512, n_t' = 40$)		`KdV` ($r = 1024, n_t' = 20$)	
VIT	0.2808±0.0006	0.3938±0.0009	0.3428±0.0012	0.6832±0.0016	0.3066±0.0003	0.5461±0.0003
MLPMixer	0.2732±0.0054	0.4259±0.0088	**0.3336**±0.0045	**0.5923**±0.0081	0.2872±0.0005	0.5235±0.0006
GFN	0.2587±0.0032	0.3490±0.0056	0.3086±0.0223	0.5952±0.0338	0.2011±0.0074	0.3464±0.0063
FNO	0.2619±0.0069	0.3849±0.0107	0.5608±0.0053	0.8424±0.0051	0.3925±0.0079	0.4623±0.0087
NFS	**0.2514**±0.0008	**0.3776**±0.00011	0.4522±0.0013	**0.6290**±0.0022	**0.2254**±0.0007	**0.0745**±0.0010
	`NS` ($r = 64, n_t' = 10$)		`NS` ($r = 64, n_t' = 40$)		`NS` ($r = 128, n_t' = 20$)	
VIT	9.3797±0.0421	12.9291±0.0703	22.8565±0.0935	29.1130±0.1428	15.7398±0.0757	20.6927±0.0664
MLPMixer	7.5246±0.0080	10.4762±0.0096	15.8632±0.0375	20.1522±0.0604	14.9360±0.0305	19.3268±0.0635
GFN	3.5524±0.0057	4.7071±0.0088	10.2250±0.0331	13.0451±0.0704	6.3976±0.00345	8.2685±0.297
FNO	3.3425±0.0007	5.2566±0.0008	8.9857±0.0010	14.0171±0.0023	4.4627±0.0004	6.3047±0.0004
NFS	**1.7425**±0.0017	**2.2847**±0.0022	**4.7882**±0.0066	**6.1508**±0.0042	**2.6988**±0.0005	**3.5121**±0.0006

Table B5: Performance comparison with Vision Mixer benchmarks on different equations ($n_t = 10$).

Vision Mixers	MAE ($\times 10^{-3}$)	RMSE($\times 10^{-3}$)	MAE($\times 10^{-3}$)	RMSE($\times 10^{-3}$)	MAE($\times 10^{-3}$)	RMSE($\times 10^{-3}$)
	`Burgers'` ($r = 512, n_t' = 10$)		`Burgers'` ($r = 512, n_t' = 40$)		`Burgers'` ($r = 1024, n_t' = 20$)	
VIT	0.5042±0.0114	0.7667±0.0225	2.4269±0.0288	3.7728±0.0431	1.5327±0.0314	2.4093±0.0408
MLPMixer	0.1973±0.0070	0.2600±0.0097	0.4210±0.0084	0.5844±0.0101	0.3303±0.0077	0.4473±0.0086
GFN	0.2383±0.0082	0.3066±0.0114	0.4187±0.0079	0.5407±0.0090	0.3500±0.0062	0.4489±0.0081
FNO	0.0978±0.0019	**0.1287**±0.0023	0.1815±0.0009	0.2410±0.0011	**0.1430**±0.0009	**0.1871**±0.0010
NFS	**0.0958**±0.0015	0.1347±0.0022	**0.1708**±0.0006	**0.2351**±0.0009	0.1474±0.0026	0.1957±0.0034
	`KdV` ($r = 512, n_t' = 10$)		`KdV` ($r = 512, n_t' = 40$)		`KdV` ($r = 1024, n_t' = 20$)	
VIT	0.2066±0.0027	0.3525±0.0049	0.2376±0.0022	0.5521±0.0036	0.1897±0.0003	0.3725±0.0009
MLPMixer	0.2152±0.0023	0.3686±0.0039	**0.2497**±0.0017	0.5400±0.0029	0.2062±0.0007	0.4429±0.0012
GFN	0.1530±0.0004	0.2607±0.0006	0.2691±0.0007	0.5451±0.0014	0.1984±0.0002	0.3869±0.0003
FNO	0.3230±0.0035	1.1105±0.0061	0.9605±0.0024	2.7500±0.0055	0.5929±0.0020	1.6473±0.0033
NFS	**0.0678**±0.0002	**0.1214**±0.0003	0.2709±0.0009	**0.5122**±0.0013	**0.1576**±0.0003	**0.3114**±0.0005
	`NS` ($r = 64, n_t' = 10$)		`NS` ($r = 64, n_t' = 40$)		`NS` ($r = 128, n_t' = 20$)	
VIT	3.9609±0.0101	6.0575±0.0250	12.3433±0.0342	16.5238±0.0415	9.3010±0.0234	14.0027±0.0380
MLPMixer	3.1530±0.0049	4.4339±0.0067	7.9291±0.0038	10.4149±0.0066	7.7410±0.0037	10.1934±0.0082
GFN	1.7396±0.0016	2.3551±0.0028	5.4464±0.0023	7.2130±0.0032	3.1261±0.0026	4.1691±0.0047
FNO	2.4076±0.0017	3.2861±0.0024	7.6979±0.0035	10.6401±0.0056	3.7001±0.0034	5.0047±0.0072
NFS	**0.8636**±0.0008	**1.2264**±0.0011	**3.1122**±0.0020	**4.1950**±0.0037	**1.8406**±0.0003	**2.5620**±0.0005

Table B6: Performance comparison with graph spatio-temporal benchmarks $(n_t = 1)$.

Graph Spatio-Temporal Models	MAE ($\times 10^{-3}$)	RMSE($\times 10^{-3}$)	MAE($\times 10^{-3}$)	RMSE($\times 10^{-3}$)	MAE($\times 10^{-3}$)	RMSE($\times 10^{-3}$)
	Burgers' ($n_s = 512, n_t' = 10$)		Burgers' ($n_s = 256, n_t' = 20$)		Burgers' ($n_s = 512, n_t' = 40$)	
DCRNN	277.8393±0.0082	346.1716±0.0088	292.1712±0.0280	368.1883±0.0204	298.4096±0.0137	373.0938±0.0186
AGCRN	289.9780±0.0001	360.9834±0.0001	272.6697±0.3404	340.1351±0.5435	305.4976±0.2120	376.0804±0.2385
GCGRU	288.4507±0.0246	361.1175±0.0512	294.9075±0.0005	367.4703±0.0004	291.0365±0.0265	365.1668±0.0827
MPPDE	24.4997±0.0014	34.5123±0.0017	25.4357±0.0002	31.7015±0.0002	25.3311±0.0004	33.7808±0.0005
NFS	**16.1860**±0.0016	**28.1504**±0.0021	**21.1634**±0.0018	**33.8976**±0.0018	**26.0818**±0.0001	**44.7962**±0.0003
	KdV ($n_s = 512, n_t' = 10$)		KdV ($n_s = 256, n_t' = 20$)		KdV ($r = 512, n_t' = 40$)	
DCRNN	1.6855±0.0001	3.0875±0.0001	3.1267±0.0001	4.8662±0.0001	5.7387±0.0001	8.3752±0.0001
AGCRN	4.0753±0.0001	6.8943±0.0001	5.4107±0.0001	9.2333±0.0001	8.4438±0.0001	13.8677±0.0001
GCGRU	1.6554±0.0001	2.6839±0.0001	3.0677±0.0001	4.6557±0.0001	5.8745±0.0001	9.4528±0.0001
MPPDE	1.5452±0.0001	2.6774±0.0001	2.9929±0.0007	5.4582±0.0010	3.0101±0.0001	4.9946±0.0001
NFS	**0.0816**±0.0012	**0.1512**±0.0022	**0.1576**±0.0007	**0.3114**±0.0018	**0.3210**±0.0021	**0.6873**±0.0049
	NS ($n_s = 4096, n_t' = 10$)		NS ($n_s = 1024, n_t' = 20$)		NS ($n_s = 4096, n_t' = 40$)	
DCRNN	30.6756±0.0001	41.7815±0.0001	52.1290±0.0138	69.7019±0.0032	88.3382±0.0864	119.5021±0.0055
AGCRN	OOM	OOM	59.9393±0.0001	79.0434±0.0001	OOM	OOM
GCGRU	28.8537±0.0019	40.1215±0.0008	49.9352±0.0028	67.5623±0.0014	85.9303±0.0731	117.9925±0.0172
MPPDE	8.9810±0.0014	12.1595±0.0022	20.7453±0.0008	32.1098±0.0018	54.2387±0.0006	90.0190±0.0007
NFS	**2.1992**±0.0021	**2.8280**±0.0033	**3.9178**±0.0054	**5.0182**±0.0080	**4.7865**±0.0042	**6.1384**±0.0069

Table B7: Performance comparison with graph spatio-temporal benchmarks $(n_t = 10)$.

Graph Spatio-Temporal Models	MAE ($\times 10^{-3}$)	RMSE($\times 10^{-3}$)	MAE($\times 10^{-3}$)	RMSE($\times 10^{-3}$)	MAE($\times 10^{-3}$)	RMSE($\times 10^{-3}$)
	Burgers' ($n_s = 512, n_t' = 10$)		Burgers' ($n_s = 256, n_t' = 20$)		Burgers' ($n_s = 512, n_t' = 40$)	
DCRNN	2.6122±0.0014	3.8435±0.0019	4.6126±0.0015	6.8853±0.0033	8.5880±0.0020	12.7394±0.0037
AGCRN	4.6667±0.0001	6.2791±0.0001	10.4900±0.0009	13.9810±0.0022	15.6143±0.0002	21.0937±0.0001
GCGRU	1.6643±0.0002	2.5074±0.0003	3.1400±0.0010	4.8008±0.0019	5.7653±0.0021	8.9335±0.0028
MPPDE	1.1271±0.0004	1.8838±0.0007	2.4554±0.0003	4.4315±0.0006	4.1213±0.0006	6.1980±0.0009
NFS	**0.1085**±0.0016	**0.1504**±0.0021	**0.1634**±0.0018	**0.2328**±0.0018	**0.1983**±0.0001	**0.2775**±0.0003
	KdV ($n_s = 512, n_t' = 10$)		KdV ($n_s = 256, n_t' = 20$)		KdV ($r = 512, n_t' = 40$)	
DCRNN	2.3196±0.0001	4.1634±0.0001	3.4503±0.0005	5.7450±0.0003	4.9286±0.0010	8.3912±0.0008
AGCRN	3.9350±0.0001	6.1166±0.0001	5.6631±0.0001	8.1191±0.0001	8.2893±0.0002	11.5684±0.0003
GCGRU	1.6643±0.0001	2.5074±0.0001	3.4205±0.0001	5.6873±0.0001	2.5032±0.0002	5.4515±0.0003
MPPDE	1.4967±0.0003	2.6309±0.0002	2.9708±0.0027	5.3811±0.0050	2.4293±0.0006	4.9310±0.0005
NFS	**0.0816**±0.0012	**0.1512**±0.0022	**0.1576**±0.0007	**0.3114**±0.0018	**0.3210**±0.0021	**0.6873**±0.0049
	NS ($n_s = 4096, n_t' = 10$)		NS ($n_s = 1024, n_t' = 20$)		NS ($n_s = 4096, n_t' = 40$)	
DCRNN	8.7025±0.0003	12.5238±0.0002	27.1069±0.0024	39.1259±0.0031	59.6602±0.0177	88.2946±0.0146
AGCRN	OOM	OOM	42.4197±0.0006	60.5375±0.0008	OOM	OOM
GCGRU	6.3570±0.0001	9.7306±0.0002	21.3537±0.0026	32.9674±0.0033	57.2493±0.0085	84.1847±0.0106
MPPDE	5.4353±0.0041	7.8838±0.0037	17.5902±0.0013	25.9372±0.0016	42.3057±0.0066	76.3374±0.0069
NFS	**0.9335**±0.0011	**1.3254**±0.0012	**1.8239**±0.0012	**2.5291**±0.0008	**3.2768**±0.0026	**4.3988**±0.0009

B.4 More Visualization

Here we provide more visualization results on the three equations. See Fig. B2, Fig. B3 and Fig. B4.

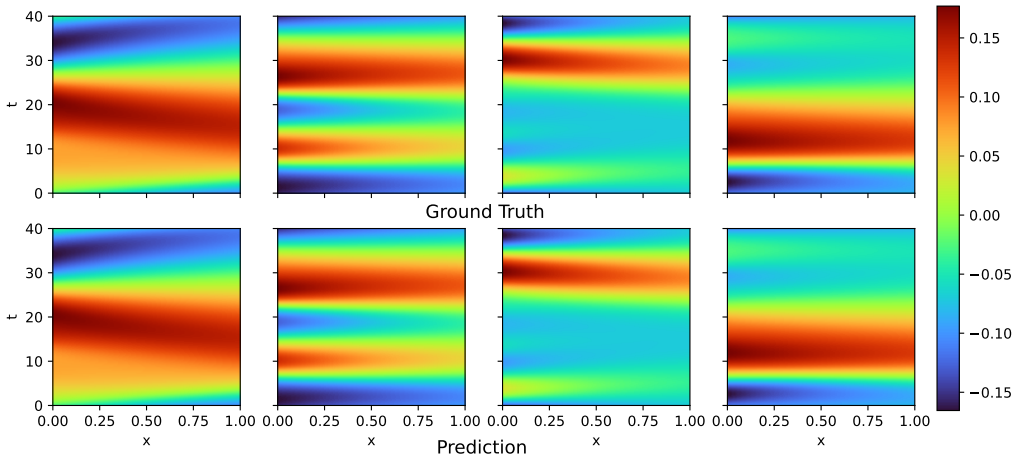

Figure B2: Visualization on equispaced Burgers' equation.

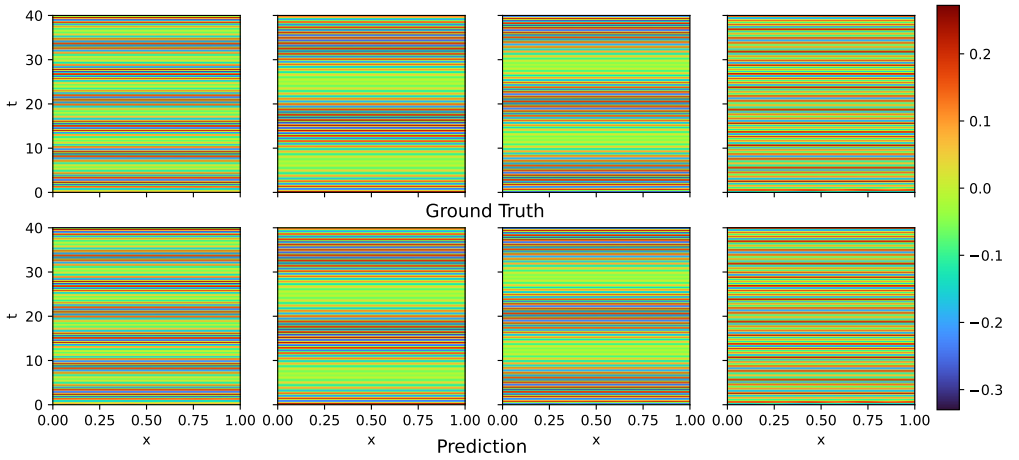

Figure B3: Visualization on equispaced KdV equation.

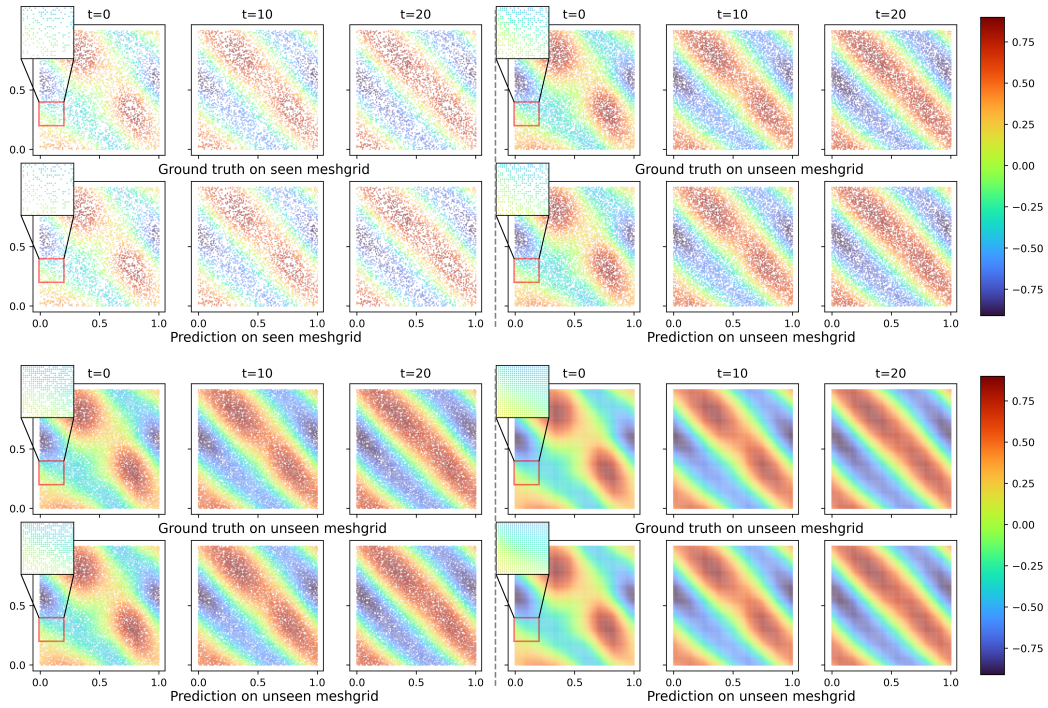

Figure B4: Visualization on non-equispaced NS equation: The training mesh ($n_s = 4096$ in upper-left) is different from the meshes in inference process ($n'_s = 8192$ in upper-right, $n'_s = 12288$ in lower-left and $n's = 16384$ in lower-right).

B.5 MESH-INVARIANT EVALUATION

Table B8: Mesh-invariant performance of NFS on Burgers' and KdV equations $(n_t = 10)$.

	MAE ($\times 10^{-3}$)	RMSE($\times 10^{-3}$)	MAE($\times 10^{-3}$)	RMSE($\times 10^{-3}$)
	Burgers' $(n_s = 512, n_t = 10, n'_t = 40)$		KdV $(n_s = 512, n_t = 10, n'_t = 40)$	
$\boldsymbol{X}$	0.1983±0.0001	0.2775±0.0002	0.3210±0.0021	0.6873±0.0049
$n'_s = 1.3n_s$	0.2371±0.0034	0.3143±0.0041	0.3769±0.0030	0.7805±0.0077
$n'_s = 1.7n_s$	0.2898±0.0113	0.3742±0.0102	0.4084±0.0072	0.8419±0.0174
$n'_s = 2.0n_s$	0.3052±0.0098	0.4180±0.0100	0.4111±0.0042	0.8471±0.0074

Table B9: Performance of NFS with its variants of NS equations $(n_t = 10)$ on unseen meshes.

	MAE ($\times 10^{-3}$)	RMSE($\times 10^{-3}$)	MAE($\times 10^{-3}$)	RMSE($\times 10^{-3}$)	MAE($\times 10^{-3}$)	RMSE($\times 10^{-3}$)
Flex + LN	NS $(n_s = 4096, n'_t = 10)$		NS $(n_s = 1024, n'_t = 20)$		NS $(n_s = 4096, n'_t = 40)$	
$\boldsymbol{X}$	0.9335±0.0011	1.3254±0.0012	1.8239±0.0012	2.5291±0.0008	3.2768±0.0026	4.3988±0.0009
$n'_s = 2n_s$	0.9731±0.0034	1.5042±0.0057	2.3530±0.0051	3.3320±0.0074	3.5439±0.0085	4.7904±0.0168
$n'_s = 3n_s$	1.1071±0.0021	1.5716±0.0038	2.5179±0.0089	3.5477±0.0125	3.6584±0.0180	4.8858±0.0246
$n'_s = 4n_s$	1.1015±0.0000	1.5627±0.0000	2.5919±0.0064	3.6526±0.0071	3.6608±0.0000	4.9521±0.0000
	MAE ($\times 10^{-3}$)	RMSE($\times 10^{-3}$)	MAE($\times 10^{-3}$)	RMSE($\times 10^{-3}$)	MAE($\times 10^{-3}$)	RMSE($\times 10^{-3}$)
Gaus + LN	NS $(n_s = 4096, n'_t = 10)$		NS $(n_s = 1024, n'_t = 20)$		NS $(n_s = 4096, n'_t = 40)$	
$\boldsymbol{X}$	1.6341±0.0034	2.1992±0.0042	2.1976 ±0.0065	3.0219±0.0090	3.6422±0.0026	5.0097±0.0039
$n'_s = 2n_s$	2.8589±0.0062	4.0562±0.0126	3.7465±0.0041	5.1308±0.0097	3.9092±0.0041	5.2402±0.0075
$n'_s = 3n_s$	3.4513±0.0168	4.5199±0.0377	5.7712±0.0123	5.7137±0.0199	4.2102±0.0082	5.5057±0.0138
$n'_s = 4n_s$	3.4357±0.0000	4.7382±0.0000	5.5990±0.0066	5.5958±0.0049	4.2628±0.0000	5.7679±0.0000
	MAE ($\times 10^{-3}$)	RMSE($\times 10^{-3}$)	MAE($\times 10^{-3}$)	RMSE($\times 10^{-3}$)	MAE($\times 10^{-3}$)	RMSE($\times 10^{-3}$)
Flex + ~~LN~~	NS $(n_s = 4096, n'_t = 10)$		NS $(n_s = 1024, n'_t = 20)$		NS $(n_s = 4096, n'_t = 40)$	
$\boldsymbol{X}$	1.2138±0.0030	1.7293±0.0047	2.5119±0.0036	3.4923±0.0058	4.2083±0.0037	5.6761±0.0092
$n'_s = 2n_s$	1.4882±0.0146	2.1681±0.0300	7.0203±0.0203	10.6096±0.0345	5.8975±0.0060	8.7704±0.0189
$n'_s = 3n_s$	1.6384±0.0088	2.4130±0.0169	7.9177±0.0059	11.9825±0.0118	6.6622±0.0063	9.5874±0.0131
$n'_s = 4n_s$	1.6975±0.0000	2.5008±0.0000	7.1962±0.0101	10.8860±0.0098	6.6951±0.0000	9.6334±0.0000

The mesh-invariant evaluation on Burgers' and KDV Equations of NFS are given in Table. B8. In Table. B8, when the spatial resolution is just 512, inference performance on unseen meshes deteriorates. This result also validate our conclusion *(2)* in the third paragraph in Sec. 4.

Besides, we give a full evaluation on mesh-invairance of NFS in NS equation, with its variants as a detailed results corresponding to Table. B9.

B.6 NEIGHBORHOOD SIZE'S EFFECTS

The effects of mean neighborhood size on the predictive performance on `Burgers'` ($n_s = 512, n_t = 10, n_t' = 40$) and `KDV` ($n_s = 512, n_t = 10, n_t' = 40$) are shown in Fig. B5.

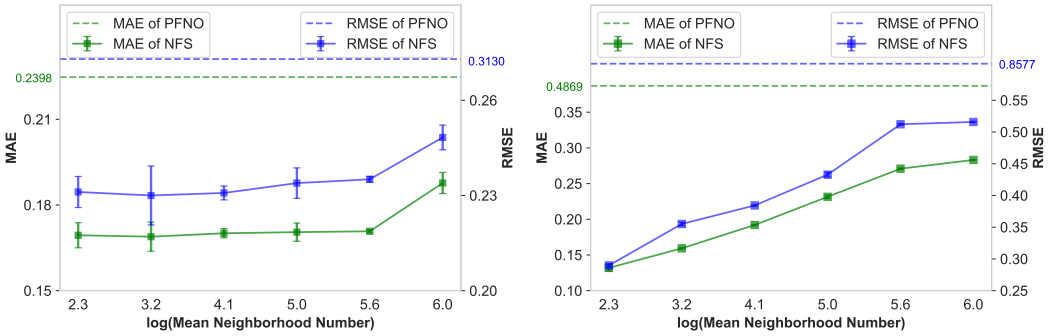

(a) `Burgers'` ($n_s = 512, n_t' = 40$). (b) `KdV` ($n_s = 512, n_t' = 40$).

Figure B5: The change of MAE and RMSE of NFS with the increase of neighborhood size on `Burgers'` ($n_s = 512, n_t = 10, n_t' = 40$) and `KdV` ($n_s = 512, n_t = 10, n_t' = 40$). PFNO is the baseline.

B.7 INTERPOLATION WITH OTHER VISION MIXERS

We conduct experiments on non-equispaced NS equations with the combination of our interpolation layers and other Vision Mixers to figure out if they can achieve camparable performance.

Table B10: Performance of different Vision Mixers combined with the interpolation layers in non-equispaced scenarios on NS equations ($n_t = 10$).

VIT	MAE ($\times 10^{-3}$)	RMSE($\times 10^{-3}$)	MAE($\times 10^{-3}$)	RMSE($\times 10^{-3}$)	MAE($\times 10^{-3}$)	RMSE($\times 10^{-3}$)
	NS ($n_s = 4096, n_t' = 10$)		NS ($n_s = 1024, n_t' = 20$)		NS ($n_s = 4096, n_t' = 40$)	
$\boldsymbol{X}$	OOM	OOM	OOM	OOM	OOM	OOM
MLPMIXER	MAE ($\times 10^{-3}$)	RMSE($\times 10^{-3}$)	MAE($\times 10^{-3}$)	RMSE($\times 10^{-3}$)	MAE($\times 10^{-3}$)	RMSE($\times 10^{-3}$)
	NS ($n_s = 4096, n_t' = 10$)		NS ($n_s = 1024, n_t' = 20$)		NS ($n_s = 4096, n_t' = 40$)	
$\boldsymbol{X}$	6.1854±0.0012	8.1556±0.0018	9.4593±0.0028	12.1316±0.0022	10.1862±0.0045	13.1548±0.0051
$n_s' = 2n_s$	8.1573±0.0126	11.2258±0.0147	12.0706±0.0132	14.9460±0.0159	10.6003±0.0127	13.6872±0.0238
$n_s' = 3n_s$	8.1952±0.0088	11.3840±0.0171	14.9910±0.0094	17.8415±0.0110	10.5633±0.0140	13.6394±0.0147
$n_s' = 4n_s$	8.7773±0.0000	11.3313±0.0000	14.9517±0.0125	17.7857±0.0199	10.5414±0.0000	13.6106±0.0000
GFN	MAE ($\times 10^{-3}$)	RMSE($\times 10^{-3}$)	MAE($\times 10^{-3}$)	RMSE($\times 10^{-3}$)	MAE($\times 10^{-3}$)	RMSE($\times 10^{-3}$)
	NS ($n_s = 4096, n_t' = 10$)		NS ($n_s = 1024, n_t' = 20$)		NS ($n_s = 4096, n_t' = 40$)	
$\boldsymbol{X}$	12.2373±0.0091	16.2902±0.0133	10.2768±0.0084	13.7852±0.0078	14.7765±0.0055	19.4872±0.0106
$n_s' = 2n_s$	13.7752±0.0164	18.3108±0.0181	17.7216±0.0225	24.1397±0.0371	15.9083±0.0235	21.0041±0.0256
$n_s' = 3n_s$	13.7054±0.0122	18.2192±0.0184	17.8238±0.0112	24.2783±0.0196	15.8986±0.0156	20.9943±0.0158
$n_s' = 4n_s$	13.7140±0.0000	18.2271±0.0000	17.8207±0.0105	24.2833±0.0141	15.8736±0.0000	20.9772±0.0000

B.8 COMPLEXITY COMPARISON

We here first give Table. B11 to show the complexity of time and memory of all the evaluated methods on NS ($r = 64, n_t = 10, n_t' = 40$).

Table B11: comparison on complexity of the evaluated methods

Type	Methods	Time/Epoch	Peak Memory	Parameter Number
Graph Spatio-Temporal Model	GCGRU	$6'18''$	8660MB	74945
	DCRNN	$9'38''$	11120MB	148673
	AGCRN	OOM	OOM	OOM
	MPPDE	$10'54''$	23333MB	622161
Vision Mixer	VIT	$3'14''$	32166MB	773217
	MLPMIXER	$1'12''$	4421MB	79749953
	GFN	$48''$	3296MB	1361729
	FNO	$27''$	3748MB	6299425
	PFNO	$43''$	3380MB	9742145
	NFS	$2'02''$	31938MB	37891937

Table B12: Detailed complexity of NFS

Interpolation on Resampled Points		
Neighbor Searching	Kernel Calculation	Weighted Summation
3522MB	3102MB	6884MB
Interpolation back on Original Points		
Neighbor Searching	Kernel Calculation	Weighted Summation
2506MB	2754MB	6884MB

It demonstrates that our method has comparable efficiency to Vision Mixers. For the graph spatial-temporal models, they suffer from the recurrent network structures and thus are extremely time-consuming while the parameter number is small, limiting their flexibility.

Time. However, once we compare the used time in PFNO and NFS, we will find that the interpolation layers are considerably time-consuming. Another module that cost time complexity is the normalization layer, as the original FNO does not include Layer-Norm in its architecture, but it is stacked in PFNO. Theoretically, PFNO handles down-sampled grids in a low resolution, because of the patchwise embedding. However, it takes more time than FNO. Therefore, we conclude that the time complexity brought from Layer-Norm is very significant, but it is affordable because of the performance improvements.

Memory. Besides, the operation of searching for each spatial point's neighborhood and calculating weighted summation in Eq. (9) and Eq. (10) are very memory-consuming. We test it on the same experiment, and give the memory usage of different models in forward process, as shown in Table. B12. The memory cost in backward process is 6902MB.

C EMPIRICAL OBSERVATION FOR THEOREM 3.1

In Sec. 3.2, Theorem 3.1 is proved to assure the expressivity of NFS. However, no further evidence gives the assurance of the convergence of the kernel interpolation. Here we conduct empirical study to give some clues.

We conduct experiments on NS equation with $n_s = 4096, n_t = 10, n_t' = 40$. In a single trial, NFS is trained with fixed meshes. We repeated the trials 10 times with different meshes, and then give the

one-v.s.-all deviations of the representation states calculated by

$$\text{Diff} = \sum_{i \neq j, i,j=1}^{10} \frac{|H_i - H_j|}{|H_i| + |H_j|}$$

where H_i is the representation states of the shape $[\sqrt{m_s}, \sqrt{m_s}, t]$. If the Diff is small in the beginning and end, it can be inferred that the interpolation kernel function converges to a similar mapping since the final predictions are close to ground truth in these experiments, and the inputs are sampled from the same instance of PDEs. We give the Diff before the first FNO and after the final of FNO layers in Table. C1. The small values indicate that the trained model usually has similar representation states. Figure. C1 and C2 give visualizations of representation states obtained by one instance of NS equation in two different trials. It indicates that the differences are getting smaller during the training.

Table C1: The defined Diff calculated by different epochs.

Epoch	$\text{Diff}_{\text{begin}}$	Diff_{end}
0	0.0676	0.0978
500	0.0102	0.0353

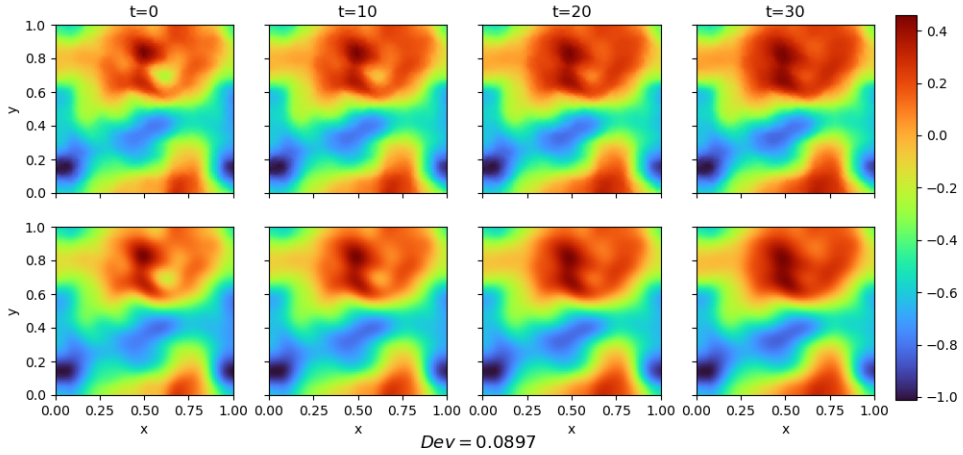

(a) Representation states at the beginning of FNO layers in two trials of Epoch 0

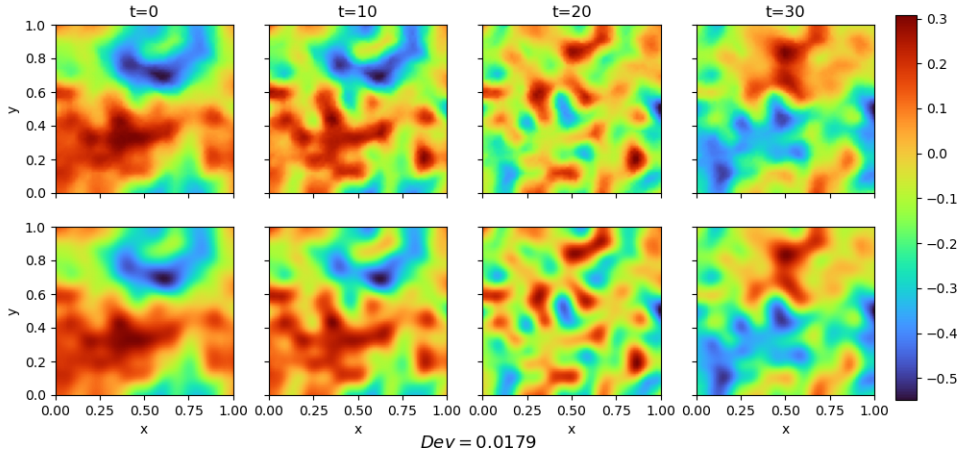

(b) Representation states at the beginning of FNO layers in two trials of Epoch 500

Figure C1: Visualization on different representation states at the beginning of FNO layers.

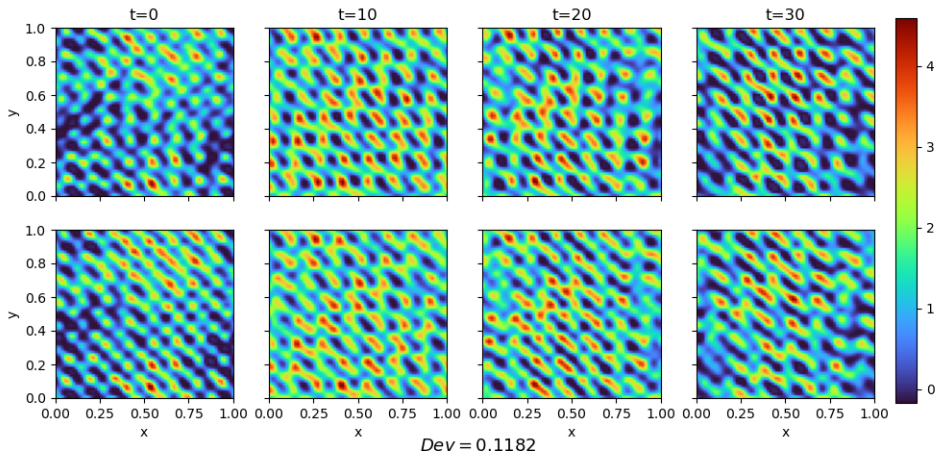

(a) Representation states in the end of FNO layers in two trials of Epoch 0

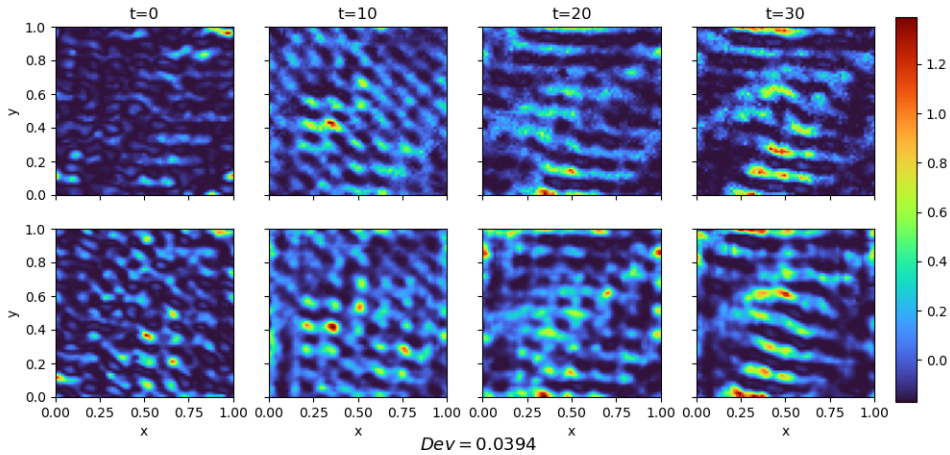

(b) Representation states in the end of FNO layers in two trials of Epoch 500

Figure C2: Visualization on different representation states in the end of FNO layers.

As a result, we present the one-v.s.-all differences of different epochs in the training process, to validate the convergence, as shown in Figure. C3.

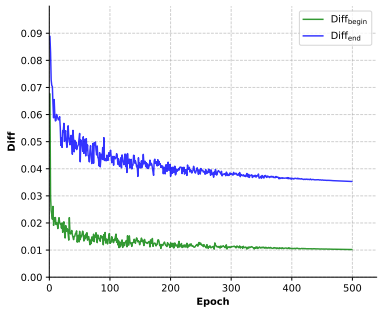

Figure C3: Convergence of Diff.